universität wien

MASTERARBEIT / MASTER'S THESIS

Titel der Masterarbeit / Title of the Master's Thesis

Order dynamics of full scale photovoltaic devices under thermal treatment and electrical bias.

verfasst von / submitted by

Nurgul Kereyeva, BSc

angestrebter akademischer Grad / in partial fulfilment of the requirements for the degree of

Master of Science (MSc)

Wien, 2023 / Vienna, 2023

Studienkennzahl lt. Studienblatt / degree programme code as it appears on the student record sheet:	UA 066 876
Studienrichtung lt. Studienblatt / degree programme as it appears on the student record sheet:	Masterstudium Physik / Master's degree programme Physics
Betreut von / Supervisor:	ao. Univ.-Prof. Mag. Dr. Bogdan Sepiol

ACKNOWLEDGEMENTS

I am deeply thankful to many people who supported me throughout this project. First and foremost, I have to thank my research supervisors at AIT, Karl Berger and Marcus Rennhofer as well as my university supervisor Professor Bogdan Sepiol. Without their assistance and dedicated involvement in every step throughout the process, their invaluable advice, continuous support, and patience during my work this thesis would have never been accomplished. I would also like to express my sincere gratitude to my wonderful colleague at AIT Gusztáv Újvári for his assistance at every stage of the research project, to Ankit Mittal and Wisnu Ananda for their insightful comments and suggestions, to Philipp Mayer-Ullmann for his support at the laboratory. I would also like to thank my family, friends and Marcus Bumbar for always being there for me.

ABSTRACT

Standardized testings of crystalline silicon terrestrial photovoltaic devices are important both for manufacturers and consumers and a key to reduce financial risks and module failures. This qualification is important to examine the impact of various stresses, such as electrical, thermal and mechanical, on the power output and lifetime of the photovoltaic systems. The aim of the present work was to study the performance stability of two photovoltaic modules with different crystalline silicon cell technologies, passivated emitter and rear cell and heterojunction, under various stabilization methods, including light- and elevated temperature-induced degradation, rapid annealing, light soaking and dark bias stabilization. Moreover, the impact of different current injection values on the ordering states of stabilization processes is presented and discussed.

ZUSAMMENFASSUNG

Standardisierte Tests von terrestrischen Photovoltaik Modulen und -Zellen aus kristallinem Silizium sind sowohl für Hersteller als auch für Verbraucher wichtig und ein Schlüssel, um finanzielle Risiken und Modulausfälle zu reduzieren. Diese Qualifizierung ist wichtig, um den Einfluss verschiedener Belastungen, wie elektrischer, thermischer und mechanischer Art, auf die Leistungsabgabe und Lebensdauer von Photovoltaikanlagen zu untersuchen. Das Ziel der vorliegenden Arbeit war es, die Leistungsstabilität von zwei Photovoltaikmodulen mit unterschiedlichen kristallinen Siliziumzellentechnologien, passiviertem Emitter und Rückseite und Heteroübergang, unter verschiedenen Stabilisierungsmethoden zu untersuchen, darunter Degradation bei Licht und erhöhter Temperatur, sowie Stabilisierung bei erhöhter Temperatur (im dunkeln) beziehungsweise bei Licht, sowie durch Stromfluss (Dark-Forward-Bias). Darüber hinaus wird der Einfluss eingeprägter Modulströme unterschiedlicher Stärke auf die Entwicklung von Stabilisierungsprozessen dargestellt und diskutiert.

Contents

List of Figures

List of Tables

1 Introduction

Crystalline silicon (c-Si) is the most commonly used photovoltaic (PV) material. Solar cells convert light energy into the electric energy by electrochemical reaction called PV effect. This energy conversion process uses the electronic properties of semiconductors [1]. Semiconductor materials have an electrical conductivity value between those of metals, such as metallic copper and insulators, such as glass. There are two basic classifications that can be used to define different semiconductor materials. Materials composed of single species of atoms from the group IV of the periodic table are the elemental semiconductors and materials build of two or more elements from special combinations of group III and group V elements are compound materials [2].

1.1 Motivation and Relevance

The world's energy market shows increasing energy demand. Fossil fuels such as coal, oil or gas together with nuclear fuels are limited and their prices will continue to rise. Furthermore carbon dioxide, one of the main contributors to global warming and greenhouse effect, is released while burning fossil fuels [1]. It is time to think about the use of renewable energy in addition to or as an alternative to fossil fuels. The production of solar cells and solar modules today is more relevant than ever, as they act as energy sources in a variety of areas, including communications, space industry, medicine, microelectronics, etc. The world population growth and technological improvements require more additional energy. The standard of living could improve if more efficient ways of producing and making use of this energy are found [3]. There is a certain indicator, the human developing index (HDI), which includes expectation of life, infant mortality, education levels etc. Alan Pasternak of Lawrence Livermore National Laboratory found a correlation between electricity consumption and the basic human well being, HDI [4] shown in Figure 1. As shown in Figure 1 the highest HDI of a given country is between 0,9 and 1,0 (North America, Australia, Japan and Europe) and the lowest HDI is 0,3 (Ethiopia). One could

easily conclude that energy is fuel for development.

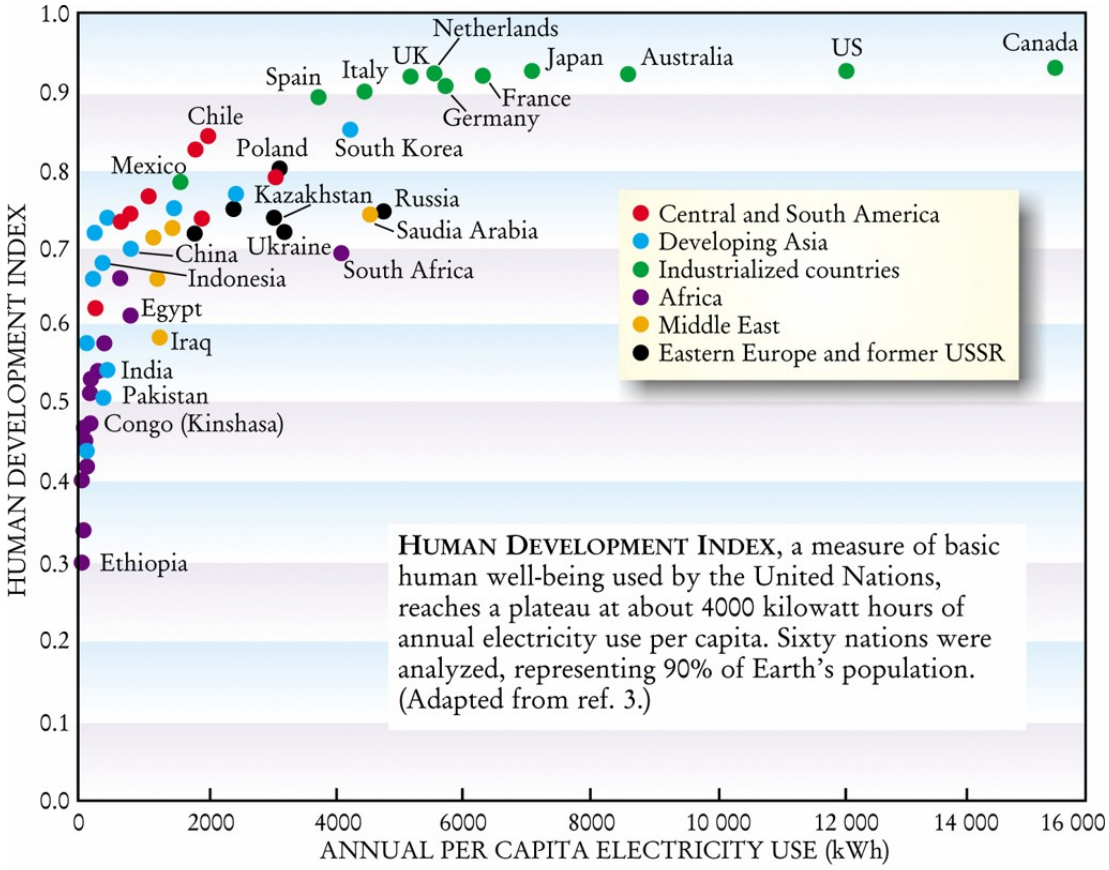

Figure 1: The graph shows the relation between HDI and per capita electricity use for selected countries [3]. Colorful dots (∘) match represented countries from the highest values in Australia, North America and Europe to the lowest in Central Africa, India and Central Asia [4].

1.2 Historical Perspective

For most people, solar energy still looks like a breakthrough made over the past decades. However, the history of the creation of solar cells as well as the research of semiconductors began in the nineteenth century. The PV effect was reported in 1839 by french scientist Edmond Becquerel. He began experimenting with electrolytic cells that generated electricity when exposed to sunlight [5]. In 1877 the PV effect was observed in solidified selenium [6]. In 1905 Albert Einstein published a paper describing the occurrence of the photoelectric effect. His theory helped explain how light quanta, photons, can generate electricity [7]. At the beginning the leading semiconductor material was germanium (Ge), but shortly after in 1960s mainly because of its better properties at room tem-

perature and economic point of view silicon (Si) easily replaced Ge. First declaration of solar cells came into play in 1954. Bell Labs scientists Daryl Chapin, Calvin Fuller, and Gerald Pearson managed to reach 6% efficiency with this first Si solar cell [8]. After that in 1957 they got a patent for a device called ”Solar Energy Converting Apparatus” that not only converted solar radiation into electricity but also made use of the solar energy to charge a storage battery [9]. Following this breakthrough solar cells were soon used for spacecrafts. In 1958, Vanguard I, the first satellite to have solar electric power, was launched [10]. However, these PV modules were too expensive for terrestrial use. The 1970s oil crisis gave rise to the new era of wind and solar power and made people invest in it. Now, in 2023, more than ever we are more conscious of the need to lower our dependence on fossil fuels.

2 Physical Background

2.1 Structure of Semiconductors

Silicon is one of the the most abundant and well studied element on the Earth. A Si atom has fourteen electrons, where the outer four are valence electrons. These valence electrons bond together and form a crystal. Solar cell is a device made up of a semiconductor materials, mostly of Si. They are obtained by converting sunlight, composed of photons with discrete amount of energy, indicating the different wavelengths of the solar spectrum, directly into electricity. Light penetrates into the cell, it can be reflected or absorbed. Absorbed photons hit negatively charged electrons in Si atoms of the semiconductor device, knock these electrons free from their atoms and force them to jump to a higher energy level. This leaves a place in the crystal structure, where the absence of an electron creates a positive charge, a ”hole”. Schematic representation of covalent bonding in a Si crystal lattice is shown in Figure 2.

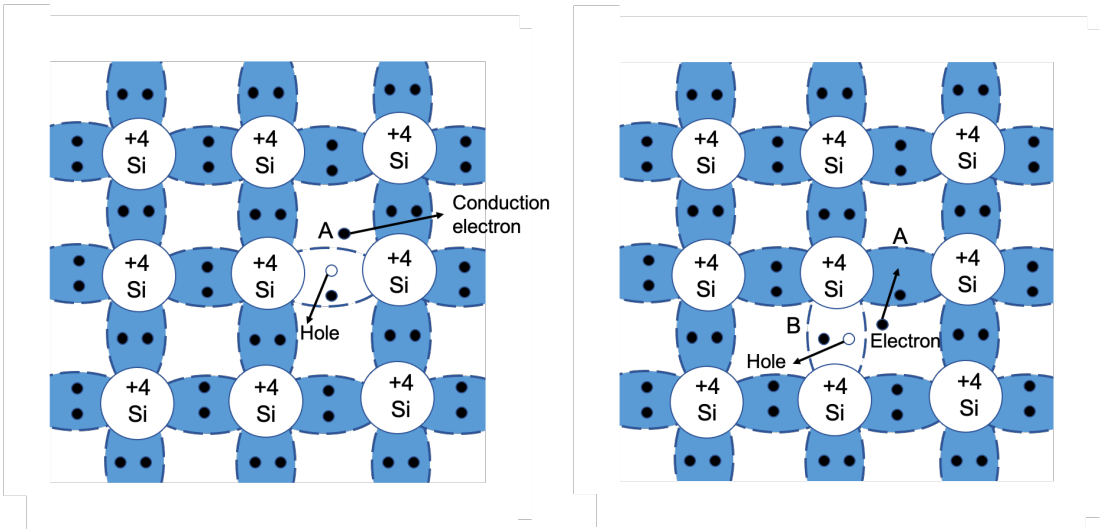

(a) A broken bond at position A

(b) A broken bond at position B

Figure 2: The picture shows a basic bond representation of intrinsic Si. In caption 2a, due to thermal energy a valence electron breaks away from the bond, leaving a hole. This vacancy may be filled with other electron, thus creating a hole movement as indicated in caption 2b. Adapted from [11].

With increasing temperature valence electrons break away from the bond creating free electrons and causing conductivity of the element. In Figure 2a we obtain the freed electron in covalent bond leaving a vacancy/hole. This deficiency may be filled up from the neighboring atom, indicating an apparent movement of the hole from position A to position B illustrated in Figure 2b. The process of occupying the position of a hole in the valence band is calling recombination. The flow of electrons that are pushed by an internal electric field from valence band into conduction band is called electric current.

2.2 Energy Bands

Electrons have discrete energy levels and occupy the lowest energy states at a temperature of absolute zero. The maximum energy level occupied by electrons in the valence band always lies below the certain energy level, the Fermi level E_F. With increasing temperature the probability that an electron occupies any energy state E is calculated via Fermi-Dirac distribution function $f(E)$, given by:

$$f(E) = \frac{1}{1 + e^{(E-E_F)/kT}} \tag{1}$$

where E_F is the Fermi level, k is the Boltzmann's constant and T is the absolute temperature [12] . The band-gap represents the amount of minimum energy needed to break a bond in semiconductor and to excite an electron from a valence band up to the conduction band. The band-gap energy E_g between the conduction band E_C and the valence band E_V is the width of the forbidden energy gap and can be written as: E_C - E_V. Depending on the classes of solids (metals, semiconductors, insulators) and on atomic structures of the same material the band-gap energy differs. The energy band representation in Figure 3 helps us to visualize and the energy band theory describes the difference between these materials [11].

Metals: Fermi level E_F lies within an allowed band.

Semiconductors: Fermi level E_F lies within a narrow forbidden band gap.

Insulators: Fermi level E_F lies within a large forbidden band [12].

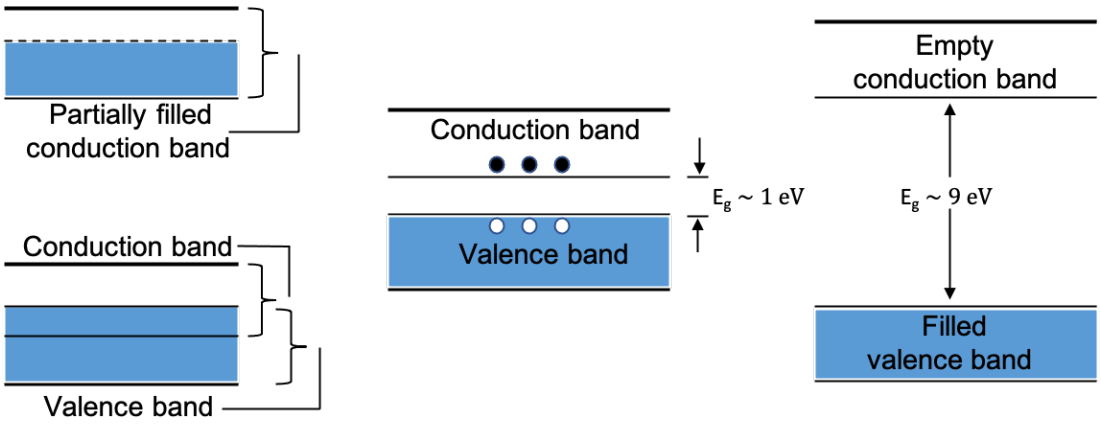

Figure 3: From left to right schematic energy band representation of a metals, where either a conduction band is partially filled (upper picture) or bands overlap (lower picture); semiconductors with a narrow gap between both bands; insulators with an empty conduction band and filled valence band, separated by a large band gap. Adapted from [11].

2.3 Doping of Semiconductors

One of the techniques to form an electric field and adjust structural and optical properties of the intrinsic semiconductors is to introduce impurities, known as "doping". The impurity is called dopant and semiconductor becomes extrinsic. Semiconductor materials from group IV can either be doped with group V or III atoms. Group V atoms are considered donors of electrons, where unbonded

electrons form n-type material. For the total amount of electrons in the conduction band per unit volume in the n-type material we have:

$$n = N_D = N_C e^{(E_F - E_c)/kT} \tag{2}$$

or equivalently

$$E_F - E_C = kTln(\frac{N_D}{N_C}), \tag{3}$$

where N_C is he effective density of states in the upper band/conduction band and N_D is the total density of donors. Group III atoms, considered acceptors, with holes form p-type material. Likewise the number of holes in the valence band per unit volume in the p-type materials is given by:

$$p = N_A = N_V e^{(E_v - E_F)/kT} \tag{4}$$

or equivalently

$$E_v - E_F = kTln(\frac{N_A}{N_V}), \tag{5}$$

where N_V is the effective density of states in the lower band/valence band and and N_A is the total density of donors. The movement of electrons results in a net charge on the atom and the p-n junction is created. In Figure 4a a Si atom is replaced by a group V atom (arsenic), the fifth electron has been ”donated” to the conduction band. Likewise, in Figure 4b a group III atom (boron) used in place of a Si atom, an extra electron is ”accepted” creating a ”hole” in the valence band [11].

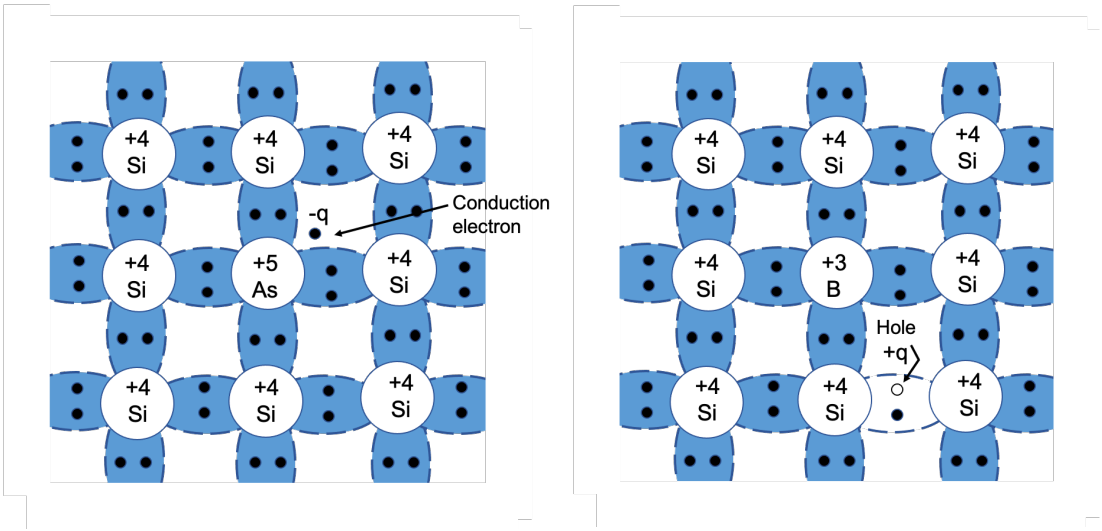

(a) n-type Si with donor (arsenic)

(b) p-type Si with acceptor (boron)

Figure 4: Schematic bond representation of a Si atom being doped with a group V atom (arsenic). As depicted in caption 4a arsenic has five valence electrons. While forming four covalent bonds with the adjacent Si atoms, one valence electron is left free. Caption 4b shows a Si atom being doped with group III atom (boron). Boron has three valence electrons and forms covalent bonds with the nearest Si atoms, leaving a vacancy/hole. Adapted from [11].

2.4 Generation and Recombination Processes

In thermal equilibrium for the idealized case of an intrinsic semiconductor electrons in the conduction band creates a ”hole” in the valence band, the density of the electrons n_e equals to the density of holes n_h. Hence:

$$n_e n_h = n_i^2 = N_C N_V e^{-E_g/kT}, \tag{6}$$

where n_i is the intrinsic density and E_g is the width of the forbidden gap between the conduction and valence bands [1]. If optical excitation or forward-biasing of p–n junction is applied and excess carriers are introduced, we have a non-equilibrium situation, where the thermal-equilibrium condition is disturbed ($n_e n_h \neq n^2$) [11]. The reverse process in which electrons from the conduction band and holes from the valence band recombine and are annihilated is known as recombination [1].

2.5 Semiconductor Junctions

By doping one region of a single semiconductor crystal with a p-type material and the other region with an n-type material forms a p-n junction. Current flow operates only in one direction in p-n junction.

In Figure 5 separated pieces of p- and n-type semiconductor materials with the corresponding energy-band diagram are shown. Near the junction, majority carriers (electrons) of the n-type material according to the Fick's first law [1] diffuse across the junction combining with majority carriers (holes) of the p-type material. Since electrons left the n-type side creating a charge imbalance, a positive space charge forms there and correspondingly, the region of the p-type material takes on a net negative charge. Transition region/space charge region/depletion region, where an electric field runs in the opposite of the natural diffusion tendency, from the positive charge in the direction of the negative charge, as seen in the lower caption of Figure 5, has been created. The hole diffusion current runs from left to right, while on the contrary the hole drift current flows from right to left. The vice versa is valid for the electron diffusion- and drift currents [11].

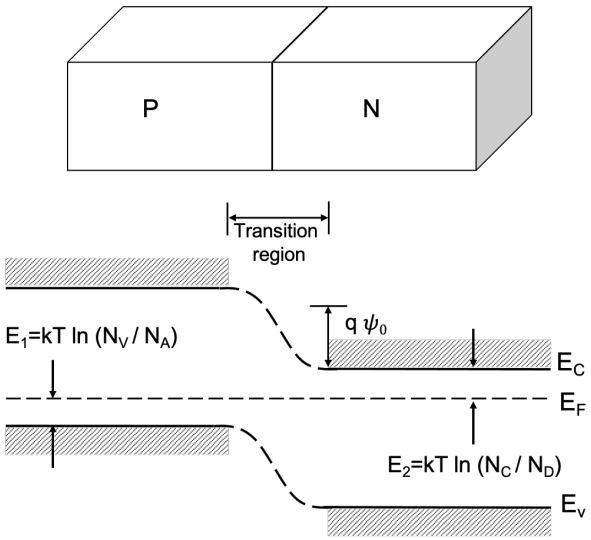

Figure 5: Separated p- and n-type regions with related energy-band diagram at thermal equilibrium. The Fermi level E_F remains constant and lies above the valence band E_V on the p-type region and below the conduction band E_C on the n-type region of the junction. Adapted from [12].

[1] Fick's law says that the rate of diffusion of a gas across a material (surface or membrane) is proportional to the concentration gradient [13].

According to Figure 5 there is a potential change ψ_0 in the transition region, with the value:

$$q\psi_0 = E_g - E_1 - E_2 \tag{7}$$

From equations 1, 3 and 5 we have:

$$\psi_0 = \frac{kT}{q} ln(\frac{N_A N_D}{n_i^2}) \tag{8}$$

2.5.1 Homojunction

A homojunction is a region between layers of similar semiconductor materials with different doping layers but with equal band-gaps. Two main types of homojunction cells are illustrated on Figure 6: the basic homojunction aluminum back surface field (Al-BSF) solar cell and passivated emitter and rear contact (PERC) cell [14]. With the anti reflective coating (ARC) improved performance of a solar cell can be obtained. Since there are various mechanisms appearing from high reflectivity value of bare silicon, which is over 30% [2], that contributes to reduction in efficiency and overall losses in solar cells, ARCs are desired [16]. The advantage and the main focus of the PERC solar cell structure is that by improving the absorption of low energy photons, back reflection enables manufacturers to achieve higher efficiencies. Low energy photons are weakly absorbed by silicon, but given a chance to be reflected back into the solar cell, they may still generate an electron-hole pair. As shown in Figure 6b the back side coating consists of three layers: the silicon oxide layer (optional, can be done by oxidation) SiO_2, which has a similar structure as silicon, thus forming a perfect interface with the silicon crystal, aluminium oxide layer Al_2O_3 covered by an insulator and the ARC silicon nitride layer SiN, which blocks the contacting of the cell with the metallization paste [14]. The representation of cross-sections of both, Al-BSF and PERC cells is shown in Figure 6.

[2] The reflectivity value is calculated from the complex refractive index listed in [15].

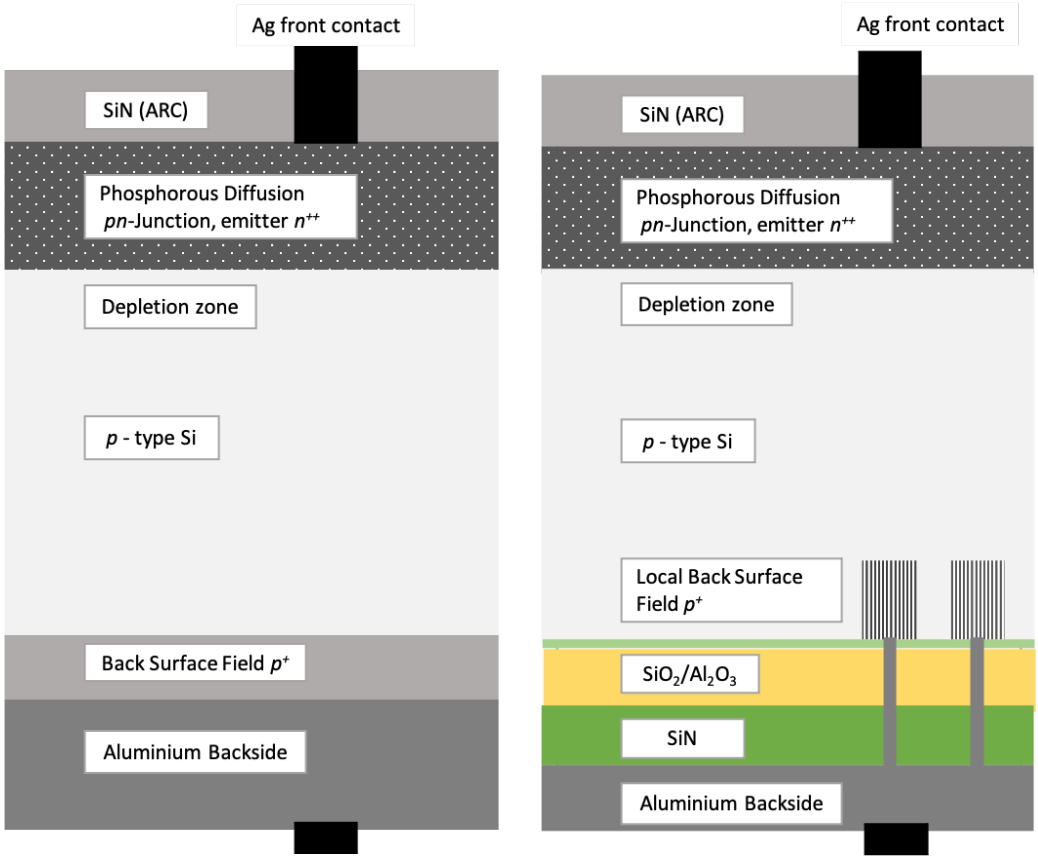

(a) Al-BSF cell (b) PERC cell

Figure 6: Schematic overview of two basic cell concepts. Caption 6a shows cross-section of an Al-BSF cell with p-type silicon. Caption 6b represents the basic concept of a PERC cell. PERC cell structure concentrates mainly on the backside of a cell. Adapted from [14].

2.5.2 Heterojunction

A heterojunction (HJT) is an area created between two regions of different semiconductors with alternating band-gaps E_g [2]. They also have different dielectric permittivities ε_s, different work functions φ_s [3] and different electron affinities $q\chi$ [4] [11]. As shown in Figure 7 HJTs are classified according to the energy-band alignment into:

type I: straddling-gap HJTs, where both electrons and holes are transferred from semiconductor A to semiconductor B and band gap of semiconductor B

[3] The energy needed to remove an electron from the exterior of a solid to the vacuum level

$$\Phi = E_{VAC} - E_F$$

[4] The energy obtained by moving an electron from the conduction band E_C to the vacuum level.

lies within the band gap of semiconductor A.

type II: staggered-gap HJTs, where electrons in semiconductor B are moved to semiconductor A, while holes in semiconductor A are moved to semiconductor B.

type III: broken-gap HJTs, where there is no transport of charge carriers between semiconductor A and semiconductor B [17], [18].

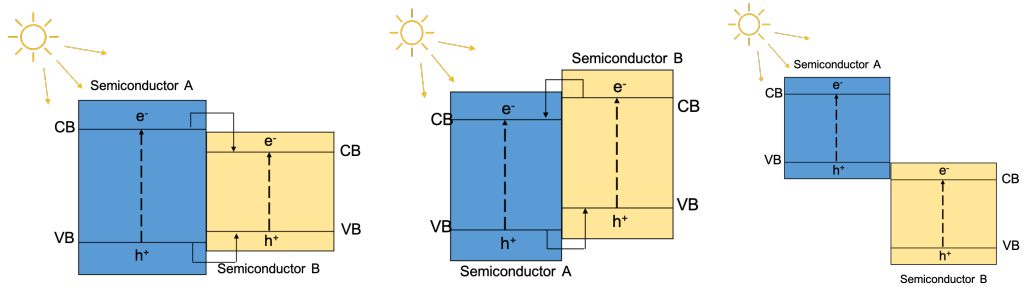

(a) Type I (b) Type II (c) Type III

Figure 7: Schematic overview of the band alignment of HJTs. Heterostructure of type I shown in caption 7a represents the configuration, where the band gap of one semiconductor material lies within the band gap of the second semiconductor material. Heterostructure of type II depicted in caption 7b illustrates staggered-gaps, where the conduction and valence bands of one semiconductor material are lower than the conduction and valence bands of the second semiconductor material. In heterostructure of type III, which is shown in caption 7c the band gaps do not overlap. Adapted from [19].

2.6 Electrostatics of P-N Junctions

2.6.1 Forward Bias

Potential difference between two regions of the junction will be shifted and no further equilibrium between diffusion- and drift current can be obtained if the voltage V_F is applied. As shown in Figure 8 due to the applied voltage the width of the depletion layer is decreased under forward bias. It allows electrons in the n-side and holes in the p-side to overcome and diffuse from one region to another as the potential barrier throughout the depletion region is reduced. Under forward bias majority charge carriers flow through the junction in opposite direction and create current flow in the forward direction.

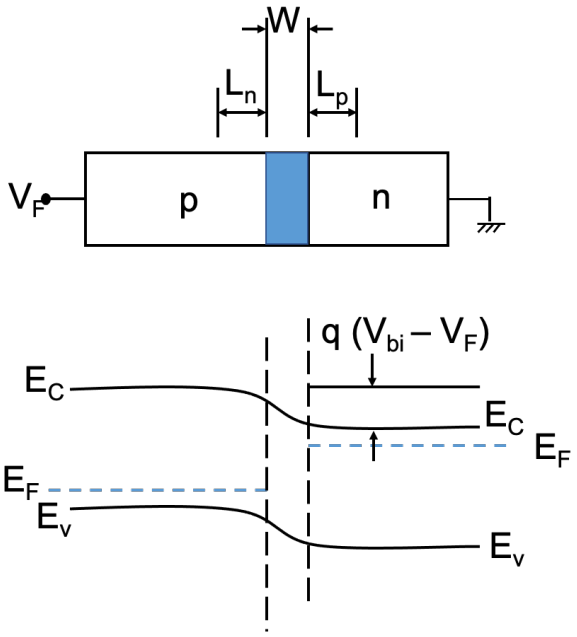

Figure 8: Schematic overview of depletion region and energy band diagram under forward bias. The depletion layer width is decreased, diffusion current increased and the built-in voltage is reduced. Adapted from [11].

2.6.2 Reverse Bias

As shown in Figure 9 under reverse bias the potential barrier increases across the depletion layer, its width grows and the electrons in n-region and holes in p-region are carried away from the junction. As a result the diffusion current is reduced. Depletion region does not contain majority charge carries thus acting as an insulator. Therefore, in theory, there should be no current flow. Nevertheless because of the low concentration of minority carriers in both regions there is still small drift current [11].

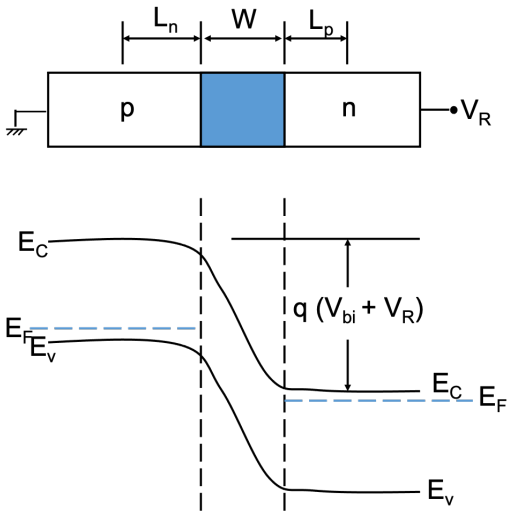

Figure 9: Schematic overview of depletion region and energy band diagram under reverse bias. The depletion layer range and the built-in voltage are increased, when reverse bias is applied. Adapted from [11].

2.7 Solar Cell Characteristics

2.7.1 Dark Characteristics

According to [12] it is reasonable to make some approximations for analysis.

1. Approximation: A diode is divided into a quasi-neutral region ($\rho = 0$) and a depletion region (carrier concentrations are negligible). This approximation is made to sharpen up the space-charge distribution.

2. Approximation: The minority-carrier concentration at the edge of the depletion layer grows exponentially with applied voltage.

3. Approximation: The minority-carrier concentration hast to be much lower than majority-carrier concentration.

4. Approximation: As long as majority-carrier currents are small, minority-carriers in uniformly doped quasi-neutral regions flow mainly by diffusion.

In n-type quasi-neutral region, hole current density J_h is:

$$J_h = -qD_h(\frac{dp}{dx}) \tag{9}$$

and respectively for electron current density J_e in p-type quasi-neutral region is:

$$J_e = qD_e(\frac{dn}{dx}), \tag{10}$$

with diffusion constant D_e for electrons, D_h for holes equivalently and charge q. The continuity equation for electrons and holes describes state of dynamic equilibrium for the density of mobile carrier electrons and holes correspondingly and is as follows:

$$\frac{1}{q}\frac{dJ_e}{dx} = U - G = -\frac{1}{q}\frac{dJ_h}{dx}, \tag{11}$$

where G is the generation rate of electron-hole-pairs and U is the recombination rate, defined as

$$U = \frac{\Delta n}{\tau_e} = \frac{\Delta p}{\tau_h}, \tag{12}$$

with associated carrier lifetimes τ_e, τ_h and Δp, Δn being the disturbances of mobile carrier holes and electrons from their equilibrium values, p_0 and n_0. After combining the hole current density equation 10, the continuity equation 11 and the carrier lifetime equation derived from recombination rate equation 12 we have:

$$D_h\frac{d^2\,p_n}{dx^2} = \frac{p_n - p_{n0}}{\tau_h} - G, \tag{13}$$

with hole density in n-type region p_{n0} and total concentration of minority-carrier holes p_n.

Setting the generation rate of electron-hole pairs $G = 0$ (dark characteristic) we have:

$$\frac{d^2\Delta p}{dx^2} = \frac{\Delta p}{L_h^2}, \tag{14}$$

where the diffusion length L_h is as follows:

$$L_h = \sqrt{D_h\,\tau_h} \tag{15}$$

Substituting the particular solution of equation with appropriate boundaries 14 in n-type and p-type regions gives:

$$\begin{aligned} J_h(x) &= \frac{q\,D_h\,p_{n0}}{L_h}\,(e^{qV/kT} - 1)e^{-x/L_h} \\ J_e(x') &= \frac{q\,D_e\,n_{p0}}{L_e}\,(e^{qV/kT} - 1)e^{-x'/L_e}, \end{aligned} \tag{16}$$

with hole density in n-type region p_{n0}, electron density in p-type region n_{p0}, applied voltage V, expansion in x-direction x and expansion in the opposite direction of x x'. As a result of the analysis above follows the derivation of the ideal diode law:

$$I = I_0 \, (e^{qV/kT} - 1), \tag{17}$$

with the expression for the saturation current density:

$$I_0 = A \left(\frac{q \, D_e \, n_i^2}{L_e \, N_A} + \frac{q \, D_h \, n_i^2}{L_h \, N_D} \right), \tag{18}$$

where A is the cross-sectional area of the diode.

2.7.2 Illuminated Characteristics

The idealized case with the uniform generation rate of electron hole-pairs is assumed. Therefore approximations from one to four of the diode in the dark are equally valid for the illuminated diode. For the n-type region setting $G \neq 0$ and assuming the boundary conditions endure unchanged gives:

$$\frac{d^2 \, \Delta p}{dx^2} = \frac{\Delta p}{L_h^2} - \frac{G}{D_h}, \tag{19}$$

with corresponding current density equation:

$$J_h(x) = \frac{q \, D_h \, p_{n0}}{L_h} \, (e^{qV/kT} - 1) e^{-x/L_h} - qGL_h e^{-x/L_h} \tag{20}$$

Thus the adapted diode law is:

$$I = I_0 \, (e^{qV/kT} - 1) - I_L, \tag{21}$$

with the light-generated current I_L:

$$I_L = qAG(L_e + W + L_h), \tag{22}$$

where W is width of the depletion layer. Graphical representation of the equation 21 can be seen in Figure 10. One can see that the IV curve is shifted down

by the current I_L into the fourth quadrant. The relevant points on the curve labeled and defined in more detail in the following section.

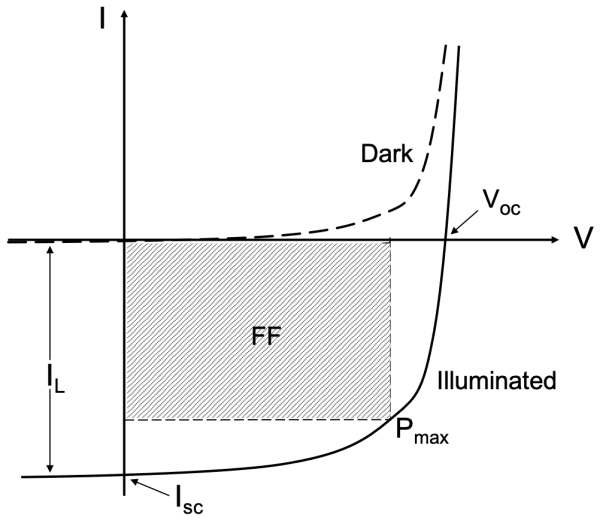

Figure 10: Properties of a solar cell in the dark and under illumination, with following IV parameters: the short-circuit current I_{sc} , the open-circuit voltage V_{oc} and the maximum power point P_{max}. The fill factor (FF) is a metric of the efficiency of a solar cell and is determined as the ratio of maximum power of the cell (P_{max}) to the product of V_{oc} and I_{sc}. Adapted from [12].

2.7.3 Current Voltage Characteristics

A current-voltage characteristics curve (IV curve) is a graphical representation of a solar cells' electrical parameters. It shows the relationship between an applied voltage and a current flowing through a cell. The main parameters to determine the performance of the solar cell are:

Short-circuit current I_{sc}: is the current at zero voltage. For an ideal solar cell $I_{sc} = I_L$.

Open-circuit voltage V_{oc}: is the voltage at zero current. An equation for V_{oc} is found by setting $I = 0$. From equation 21 we have:

$$V_{oc} = \frac{kT}{q} ln\left(\frac{I_L}{I_0} + 1\right) \tag{23}$$

Fill factor FF: is the ratio of the rectangular areas formed by the point of origin and the maximum power point to the one determined by open circuit voltage

and short circuit current. Graphically FF represents the "squareness" of the solar cell.

$$FF = \frac{P_{max}}{V_{oc} I_{sc}} \tag{24}$$

3 Methodology

3.1 Measurement Devices

3.1.1 Solar Simulator

A solar simulator provides accurate, collimated beams and is used for characterization of photonic properties. According to its performance a solar simulator is classified by the international electrotechnical commission (IEC) standard 60904-9 and is divided into three classes: A, B or C in each of three categories: spectral content, spatial uniformity and temporal stability. There are also two main types of solar simulators: pulsed, where arc lamps create a light pulse with the time span under one second and continuous, with different types of lamps, so that there is a constant light for numerous hours [20]. Manufactured by Pasan, the HightLIGHT solar simulator is a Class A+A+A+ type pulsed solar simulator we used for current-voltage characteristics curves and power measurements. The uncertainty of the current-voltage measurements is 0,1 %.

3.1.2 DragonBack

Highly efficient and highly capacitive modules with back-contact and HJT solar cells in pursuance of costs reduction have been developed. Unfortunately, the performance at standard test condition (STC) [5] for such modules cannot be measured within one 10 ms flash with a standard voltage ramp and as a result there are measurements artifacts. In order to avoid these artifacts ei-

[5] The Standard Test Conditions for a PV module are at 1000 W/m^2 irradiance under 1.5 air mass (AM) solar spectrum and at 25°C module temperature.

ther a steady state sun simulator or subsequent flashes (multiflash method) is needed to be able to increase the IV sweep time [21]. DragonBack is a method developed by Pasan SA, which is based on a dynamic sweep of the voltage ramp in a series of steps that allow to apply customized voltage profile within one 10 ms flash pulse without having any measurements artifacts. The module 190511129100003Q17el manufactured by Hevel is highly capacitive module, thus we used the DragonBack method to do electrical performance at STC. These devices in fact usually require a steady-state solar simulator or pulse duration longer than 100 ms.

3.1.3 Climatic Chamber

Climatic chambers for testing PV modules are used to put any given product under customized stress conditions. These particular conditions are created and controlled within the chamber. In order to keep our samples at constant temperature during different test, they were put into climatic chamber. This environmental chambers typically have a temperature range from a minimum of -40 to -80°C to a maximum around 300°C. For our testing protocols after the chamber reached 75°C the bias voltage was started for the duration of several hours, depending on stabilization methods. Climatic chamber's temperature fluctuation is approximately ±1°C of the set target temperature.

3.2 Modules

Two different samples were used for the experiments: HJT module with serial number: 190511129100003017el manufactured by Hevel and homojunction module with serial number: 002005342000406E manufactured by Energetica. Pictures of technical datasheets of both modules with images of the modules' front side are shown in Figure 11. Details of these types of junctions were introduced in section 2.5. Table 1 provides a brief description of the samples and table 2 contains information about electrical properties stated in the manufacturers' datasheets.

Table 1: Characterization of the samples

Manufacturer	Serial number	Technology
Energetica	002005342000406E	homojunction Mono c-Si
Hevel	190511129100003Q17el	heterojunction Mono c-Si

Table 2: Solar panel technical datasheet

Sample	V_{oc} [V]	I_{sc} [A]	P_{max} [W]	V at P_{max} [V]	I at P_{max} [A]
002005342000406E	40,50	10,34	310	33,15	9,50
190511129100003Q17el	43,6	9,2	310,8	35,9	8,7

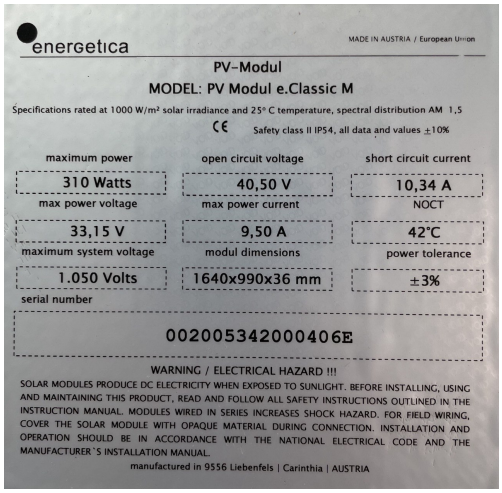

(a) e

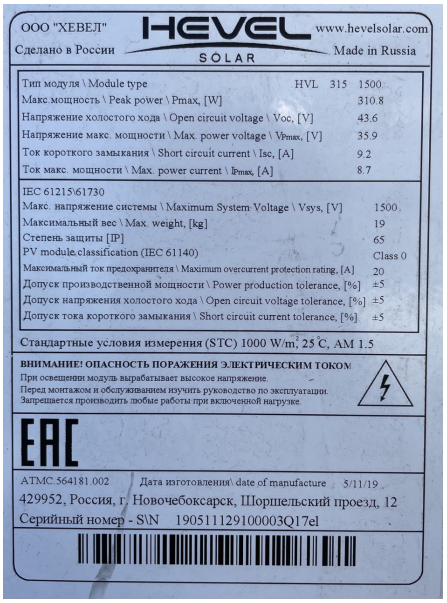

(b) h

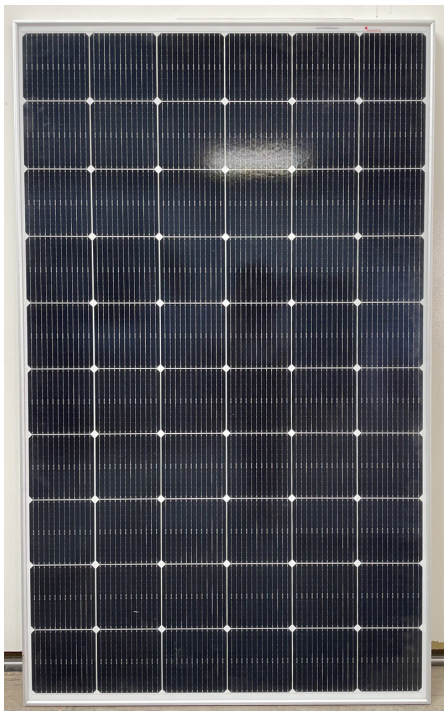

(c) e

(d) h

Figure 11: From left to right: captions 11a and 11b represent the images of the datasheets of Energetica and Hevel modules. Captions 11c and 11d illustrate the images of the Energetica and Hevel modules' front side.

3.3 Electroluminescence Imaging

Electroluminescence (EL) is an optical and electrical phenomenon, where the conversion of electrical energy into non-thermal emitted light caused by radia-

tive recombination of carriers occur at a p–n junction. EL is widely used to analyse the quality of the electrical contacts of solar cells and to observe micro cracks and other defects within the solar cell material [22]. EL uses a solar module as an infrared diode emitting light in the near-infrared (NIR) spectrum. The EL technique is non-destructive and provides real time, relatively fast and high resolution images with a 2D distribution of the characteristic features. According to the IEC technical specification [23] PV modules are measured with a power supply under forward bias condition. The required voltage is in the range of the open circuit voltage. A silicon charge coupled device (CCD) camera detects produced photoemission.

3.4 Stabilization Methods

3.4.1 LeTID

Light- and elevated temperature-induced degradation (LeTID) is a form of a solar cell degradation seen in almost all types of c-Si wafers and solar cells. First observed by Ramspeck et al. in 2012 [24] and then confirmed by Fertig et al. [25] the degradation is not caused by the light induced degradation (LID) mechanisms and is neither based on boron-oxygen complex formation, nor on iron-boron pair dissociation processes.While the main reason of the LeTID defect is still unknown, three possible state transitions of the LeTID defect have been proposed [26, 27, 28] and are shown in Figure 12.

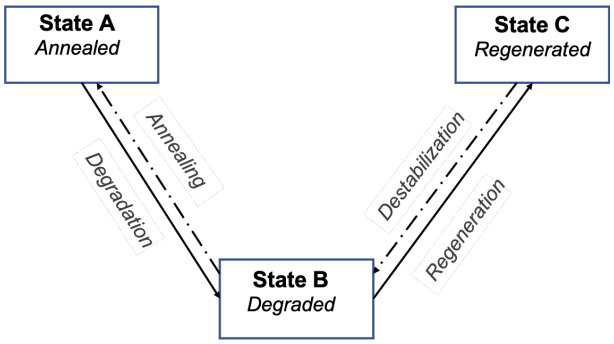

Figure 12: Schematic overview of three-model state for the LeTID defect, which can be obtained in an annealed, degraded or regenerated states [29]. Adapted from [30].

Degradation (AB) is carrier-induced and depends on the temperature and injection conditions [31]. Bredemeier et al. have shown that the degradation rate constants can be described by an Arrhenius law [32].
Regeneration (BC) is more slowly and strongly depends on higher temperature and higher injection current. Both regeneration and degradation are accelerated by the same factors thus happening simultaneously [29].

After various of LeTID tests for different modules Fokuhl et al. have shown that a testing standard plays an important role [33]. Based on LeTID round robin [34] and an internal standard by technischer überwachungs-Verein (TÜV) Rheinland (2 PfG 2689/04.19) a technical specification (TS) for IEC standardization has been developed. According to [35] in order to activate LeTID we need injection of electrical current at high temperatures. Testing sequential order is as follow in Figure 13.

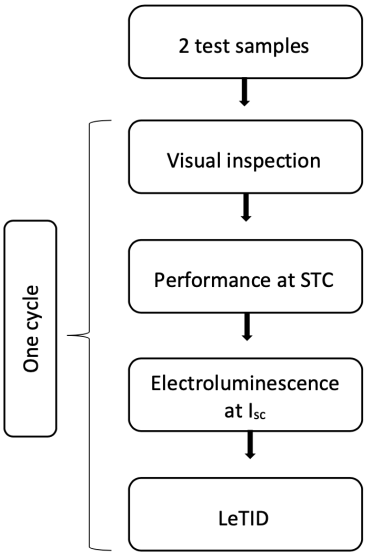

Figure 13: Schematic overview of the applied LeTID cycle for both modules. The test sequence begins with visual inspection and ends with one full LeTID round of (162 +8/-0)h in a dark climatic chamber. Adapted from [35].

Our PV *module samples* were not intentionally engineered to be LeTID-sensitive PERC modules. They were stored in the dark at 25 ±3°C and have underwent quality control.
Visual inspection (module quality tests (MQT) 01) of IEC 61215-2 is used to identify major visual defects such as cracks, bubbles or delaminations, etc.
Performance at Standard Test Conditions (MQT 06) of IEC 61215-2 is used to

specify the electrical performance of the PV modules at 1000 W/m^2 irradiance under 1.5 AM solar spectrum and at 25°C cell temperature.
EL was measured at forward bias at I_{SC} and 0,1 I_{SC}. Different injection values are important to recognize the root-cause of the observed defects.
LeTID requires two main phases: degradation followed by regeneration. The first phase was performed under 75°C, which allows LeTID to progress slowly enough to observe maximum degradation, at 2($I_{SC\,initial}$ - $I_{MPP\,initial}$) ± 1% for (162 +8/-0)h in a dark climatic chamber. The main goal of the second phase is to achieve the regenerated state with increased temperature (85°C) and higher injection level for (500 +24/-0)h in a dark climatic chamber. Each of the phases is followed by STC IV curve measurements and EL imaging at forward currents of I_{SC} and 0,1I_{SC}. The degradation phase has to be repeated until the module power was stable and was no longer decreasing and vice versa for the regeneration phase. As reported in [34], in practice, following the existing protocol [35] is not always leading to desired results. Unfortunately, we had little insight into wafer type and device architecture except for the solar panel technical datasheet. Given the module history, measurements procedures, stabilization time and different experimental routes it was not possible to achieve the regeneration phase.

All LeTID measurements were executed and controlled via Arduino. A platform, which constits of a physical programmable circuit board (microcontroller) and a software (integrated development environment). Both, software and microcontroller were provided by austrian institute of technology (AIT). In order to read and plot the data from Arduino a python code was written by me.

3.4.2 Thermal Annealing

Temperature is a key stress factor that directly affects, causing order-order, order-disorder or disorder-order transitions within the samples, the performance of a PV module [36]. The modules were put in the dark chamber at annealing temperature of 85°C for 24 h. Since the samples did not achieve the regeneration phase, thermal annealing (TA) followed by light soaking (LS) were intro-

duced.

3.4.3 Light Soaking

Extended duration illumination (LS) causes changes in the device performance and gives rise to either metastable electrical or structural effects. Depending on electrical bias, temperature etc. LS has a great impact on both initial and long-term stabilized device performance [37]. In our experiments the samples were exposed to an irradiance of 1000 W/m^2 for 20 h at 50°C. An IV characteristic curve was measured in a pulsed solar simulator under STC conditions before and after both TA and LS.

3.4.4 Electrical Bias Stabilization

Alternative stabilization procedures, which include preconditioning and degradation protocols are crucial for further understanding of correlation between cell structure and power output. One of the methods to maintain the module performance is to apply forward bias current injection alternatively to light exposure. Under forward bias the Fermi level is shifted, so that defect states populate resulting order-disorder transition (degrading) or they depopulate following order-order transition (stabilizing) [38]. As described by Ananda et al. [36] there is a relationship between the systemic current-induced degradation (order–disorder) with the process of stabilization changes (order–order) of the sample. Relatively low bias current injection level was used to avoid such interaction. Different biasing routes are shown in tables 3 and 4. The temperature was set to 75°C. To reduce stress on the modules, we started with relatively low forward bias and as soon as we saw plateau curve we added the fractions 1/3 of the I_{SC} for the next biasing round. Each of the modules was maintained at forward bias varying between short-circuit currents of 0,33 I_{SC} and 1,67 I_{SC} for three hours as soon as the temperature was stable at 75°C (±1°C). After three hours the bias current was turned off and the temperature was brought back to 25°C. IV characteristics were taken after each cycle for both modules

using the Pasan solar simulator under STC. In austrian institute of technology (AIT) laboratory it was possible to run a maximum of two cycles per workday. Modules were stored at room temperature in a dark chamber between shifts of bias testing.

Table 3: Overview of stabilization procedures of 002005342000406E (Energetica)

Stabilization method	Amount of cycles	Temperature [°C]	Duration of each cycle [h]
LeTID	3	75	163
Thermal annealing	1	85	24
Light soaking	1	50	20
Bias at 0,33 I_{SC}	1	75	3
Bias at 0,67 I_{SC}	3	75	3
Bias at 1,0 I_{SC}	8	75	3
Bias at 1,33 I_{SC}	7	75	3
Bias at 1,67 I_{SC}	3	75	3

Table 4: Overview of stabilization procedures of 190511129100003Q17el (Hevel)

Stabilization method	Amount of cycles	Temperature [°C]	Duration of each cycle [h]
LeTID	3	75	163
Thermal annealing	1	85	24
Light soaking	1	50	20
Bias at 0,33 I_{SC}	1	75	3
Bias at 0,67 I_{SC}	3	75	3
Bias at 1,0 I_{SC}	5	75	3
Bias at 1,33 I_{SC}	6	75	3
Bias at 1,67 I_{SC}	2	75	3

3.5 Arrhenius Behaviour

Arrhenius' behaviour curve is used to illustrate a temperature dependence of reaction rate constants. As it is valid for all mechanisms following Boltzmann statistics of energy distribution we illustrated a short circuit current dependence [39].

3.6 Computational Analysis

A self-written Python program was used for analysis and visualization of data for the LeTID experiment.

3.7 Errors

Pasan sun simulator was calibrated everyday by measuring a reference module to detect any deviation in the electrical performance of the reference module. The deviation in I_{sc} and V_{oc} values had to be below 0,5% in comparison to the previous calibrated values. Since the accuracy of this calibration was less than 0,01% in the absolute values the errors of the IV characteristics data are neglected in the present work.

4 Results

In this chapter the main results of the experiments, which are mentioned in the methodology are described in details. The results are sorted by the standardization method, LeTID in section 4.2, the alternative stabilization methods 4.3 (TA, LS) and electrical bias in section 4.4. The discussion of the presented results and their interpretation are given in the next chapter.

4.1 Specimen

For our experiment, two PV modules with different c-Si cell technologies (PERC and HJT) from two different manufacturers underwent various stabilization methods explained in section 3. Both modules were treated almost similarly, varying only the number of cycles needed to reach stabilization criterion. The exception was the electrical bias stabilization of Hevel module (190511129100003Q17el), in order to be able to observe other mechanisms between R2 and R3 at 1,33

I_{sc} we stopped injection of forward bias for two months and applied only thermal stress for ten rounds. Electrical characteristics of both modules are listed in table 5, corresponding IV characteristics curves at STC are shown in Figure 14.

Table 5: Initial electrical parameters at STC for both samples. Multiflash measurements were done for Energetica module and DragonBack method was applied to Hevel module

Sample	V_{oc} [V]	I_{sc} [A]	P_{max} [W]	V at P_{max} [V]	I at P_{max} [A]	FF [%]
002005342000406E	40,57	9,69	307,8	33,28	9,25	78,27
190511129100003Q17el	43,42	9,11	303,9	35,74	8,51	76,81

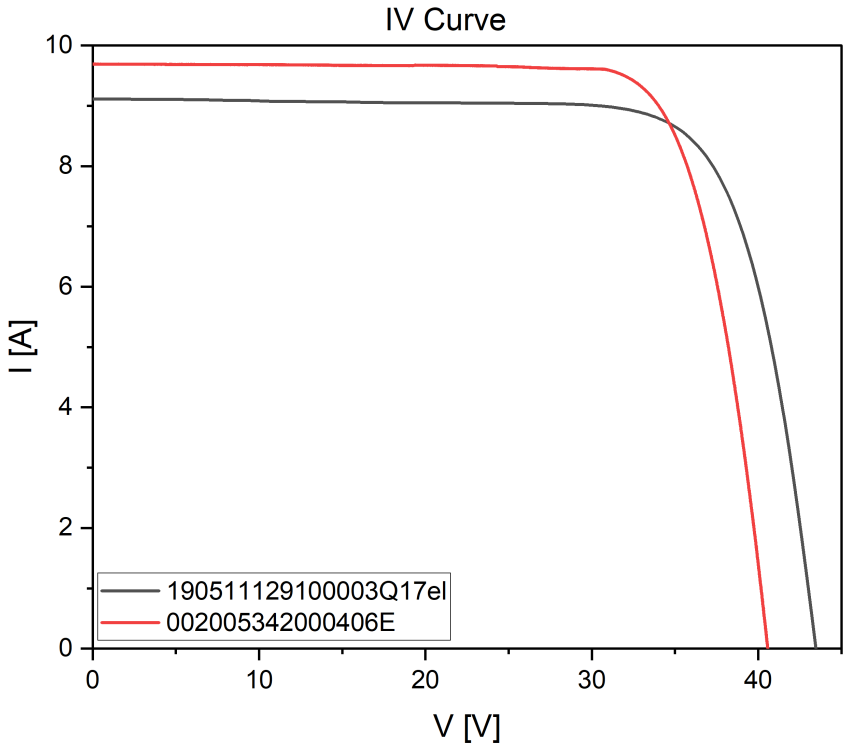

Figure 14: Initial IV characteristic curves at STC for both modules. Multiflash measurements were done for Energetica module and DragonBack voltage profile was applied to the Hevel module for the measurement of the IV curve.

STC measurements were followed by EL imaging shown in Figure 15 at forward current of I_{sc}.

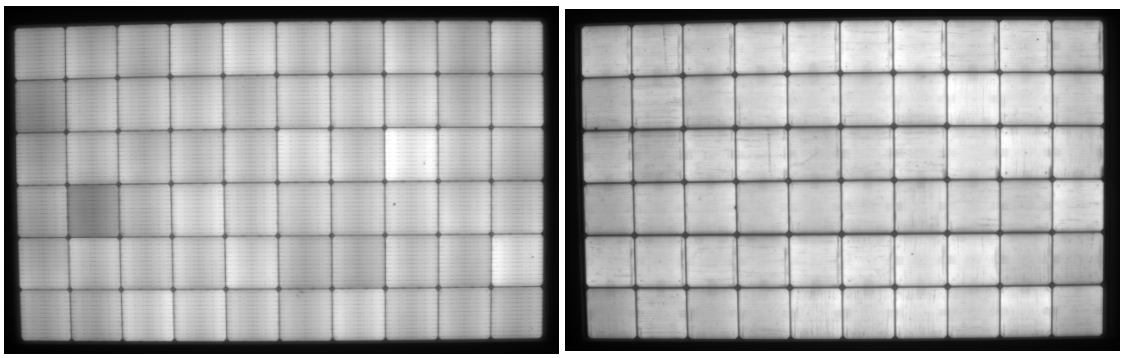

(a) 002005342000406E (b) 190511129100003Q17el

Figure 15: EL images taken at I_{sc} for both modules before any stabilization procedures. Pixel values are not changed, only the brightness and contrast are adjust for sharpening the images.

In graphs 16a and 16b in Figure 16, the first part (roughly 500 h) represents power change in LeTID procedure. The second part, set side by side to LeTID, is from approximately 500 h to 650 h shows absolute power evolution during other stabilization methods, including TA, LS and bias stabilization.

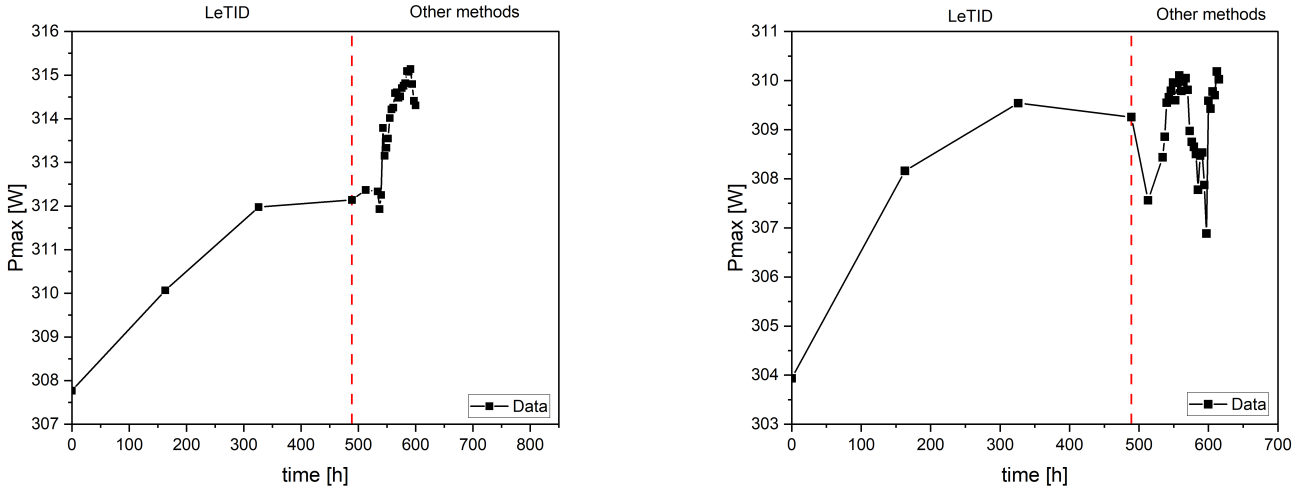

(a) 002005342000406E (b) 190511129100003Q17el

Figure 16: Power evolution of both modules during exposure time in LeTID testing procedure and other stabilization methods, including TA, LS and forward bias stabilization. The lines black are for guidance of the eyes. The dashed red lines are for visual separation of stabilization methods.

4.2 LeTID

Electrical parameters for both modules after every LeTID round are summarized in table 6 and IV characteristic curves, which are almost indistinguishable in this type of data representation are shown in graphs 17a and 17b in Figure 17. The relative changes of the STC performance of both modules are also plotted in graphs 18a and 18b in Figure 18. These plots illustrate the relative change of various parameters' output at STC after almost 500 h of stress for both modules. After nearly 3 weeks of stress there were no significant changes in power output compared to [34]. The samples did not reach the point of saturation and also did not enter the regeneration phase as reported in LeTID round robin [34] As depicted in Figure 18a the largest relative change of 0,67 % of Energetica module can be seen in P_{max}, followed by 0,6% change in V_{oc}. Fill factor has the smallest relative change of 0,31%. Hevel module has the largest relative change of 1,75% in P_{max}, with 0,73% relative change in V_{oc} afterwards and with 0,47% in I_{sc}

Table 6: Electrical parameters at STC after every LeTID round for both modules. Multiflash measurements were done for Energetica module and DragonBack method was applied to Hevel module

Sample	V_{oc} [V]	I_{sc} [A]	P_{max} [W]	V at P_{max} [V]	I at P_{max} [A]	FF [%]
002005342000406E MQT02	40,57	9,69	307,8	33,28	9,25	78,27
002005342000406E R1	40,74	9,71	310,1	33,48	9,26	78,38
002005342000406E R2	40,82	9,73	312	33,62	9,28	78,54
002005342000406E R3	40,82	9,74	312,1	33,6	9,29	78,51
190511129100003Q17el MQT02	43,42	9,11	303,9	35,74	8,51	76,81
190511129100003Q17el R1	43,75	9,14	308,2	36,2	8,51	77,1
190511129100003Q17el R2	43,83	9,15	309,5	36,32	8,52	77,21
190511129100003Q17el R3	43,73	9,16	309,3	36,22	8,54	77,22

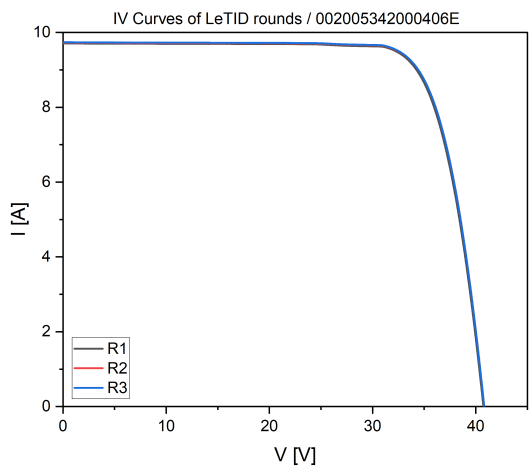

(a) 002005342000406E

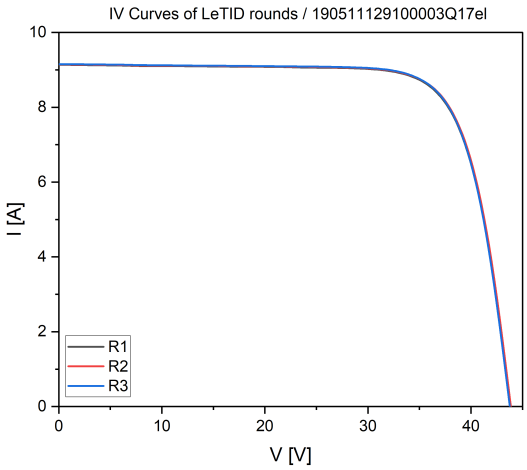

(b) 190511129100003Q17el

Figure 17: IV characteristic curves for both modules under STC conditions after every LeTID cycle. To measure the electrical performance of Hevel module at STC illustrated in graph 17b the DragonBack method was used. As the changes in electrical parameters are very small, all three IV curves for each module look very similar.

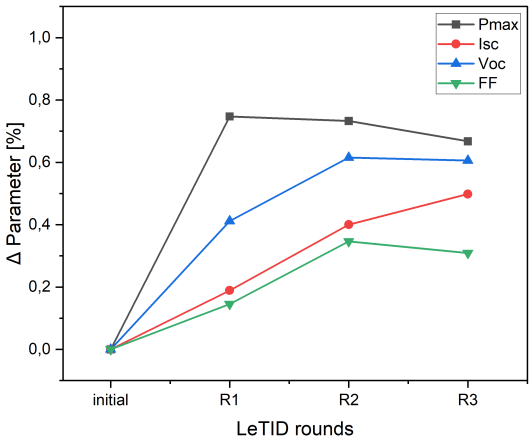

(a) 002005342000406E

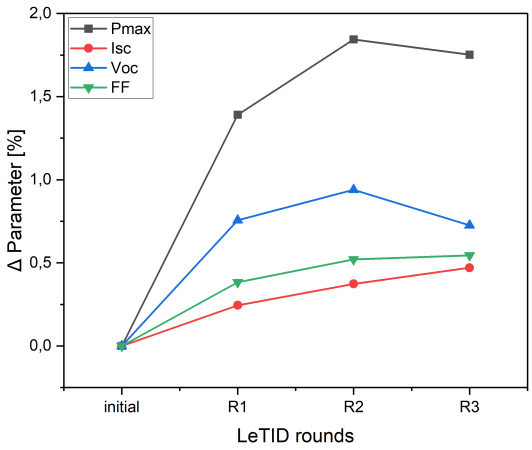

(b) 190511129100003Q17el

Figure 18: Relative changes of STC performance parameters of both modules during LeTID testing. The largest relative change of 0,67% is in P_{max} (■), followed by 0,6% in V_{oc} (blue ▲) for Energetica module. Similarly for Hevel module, the largest relative change of 1,75% is in P_{max} (■), followed by 0,73% in V_{oc} (blue ▲). The lines are for guidance of the eyes.

The largest relative change is in P_{max}, followed by V_{oc} for both samples. Captions mentioned in Figures 17 and 18 are derived from the measurement in Pasan flasher with multiflash measurements method and DragonBack approach accordingly. In order to monitor parameter changes during LeTID stress

and be able to detect degradation earlier, dark IV in-situ measurements were performed. Dark IV in-situ measurements is another technique to gain information about module performance during an ongoing stress test. Current and voltage changes detection with changing stresses but without interrupting the procedure can be observed via this method. The graph 19a in Figure 19 represents dark IV curve of sweep N21, plotted using data from the IV dark in-situ measurement method. The periodicity of every IV-Sweep is 10 min. As shown in Figure 20 after each 10 min for roughly 8 s the current is at its maximum of approximately 10 A for 002005342000406E and respectively for roughly 11,6 s at approximately 10,4 A for 190511129100003Q17el. This repetitive high current flow may accelerate the LeTID degradation speed. Logarithmic plot of both modules can be seen in Figure 19b. Some disturbances with module manufactured by Hevel are obtained. As found further they arose from the power supply we used for the second channel. As soon as we changed the power supply, disturbances disappeared.

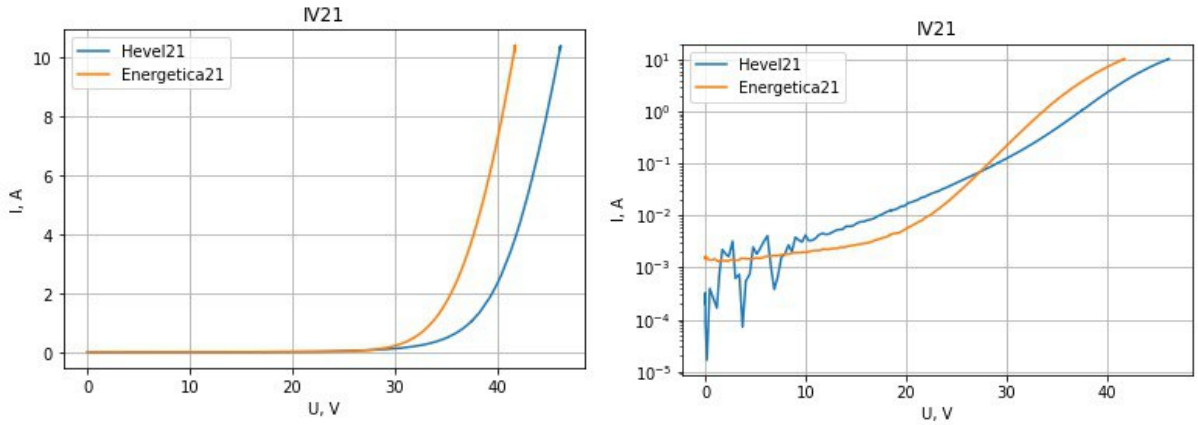

(a) IV characteristic curve of dark IV in-situ measurement of sweep N21

(b) Logarithmic representation of IV characteristic curve of dark IV in-situ measurement of sweep N21

Figure 19: Caption 19a illustrates IV characteristic curve of dark in-situ measurement of sweep N21 in the first LeTID round. Its logarithmic representation is obtained in caption 19b. Sweep N21 is chosen arbitrarily.

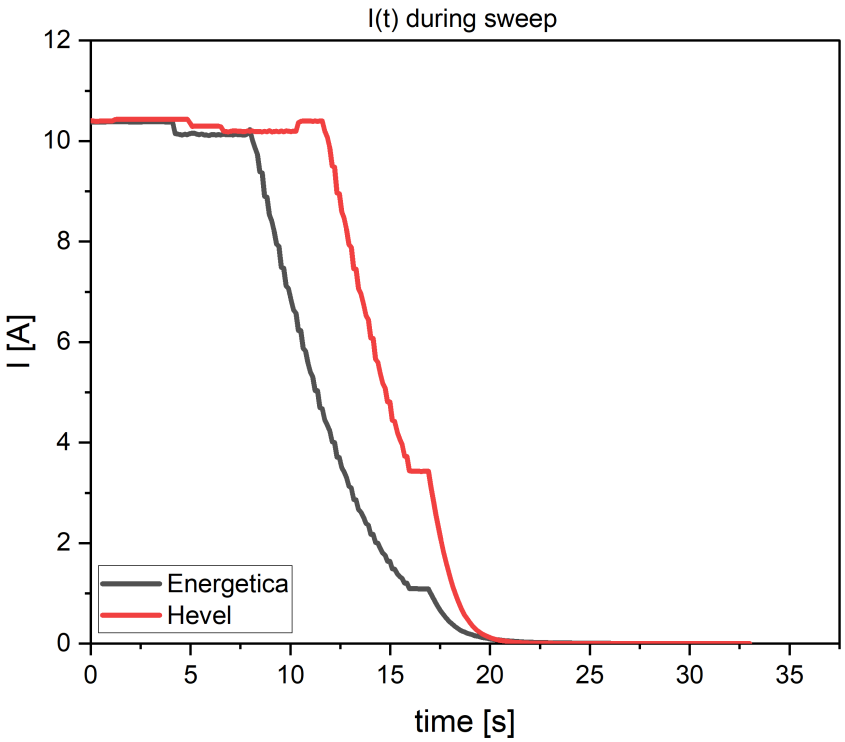

Figure 20: Graph shows the current flow during dark in-situ measurement of sweep N21 over time in the first LeTID round for both modules.

STC and dark IV in-situ measurements were followed by EL imaging shown in Figure 21 at forward currents of I_{sc} and 0,1 I_{sc}. No visible changes in EL images after LeTID rounds compared to initial EL images were obtained.

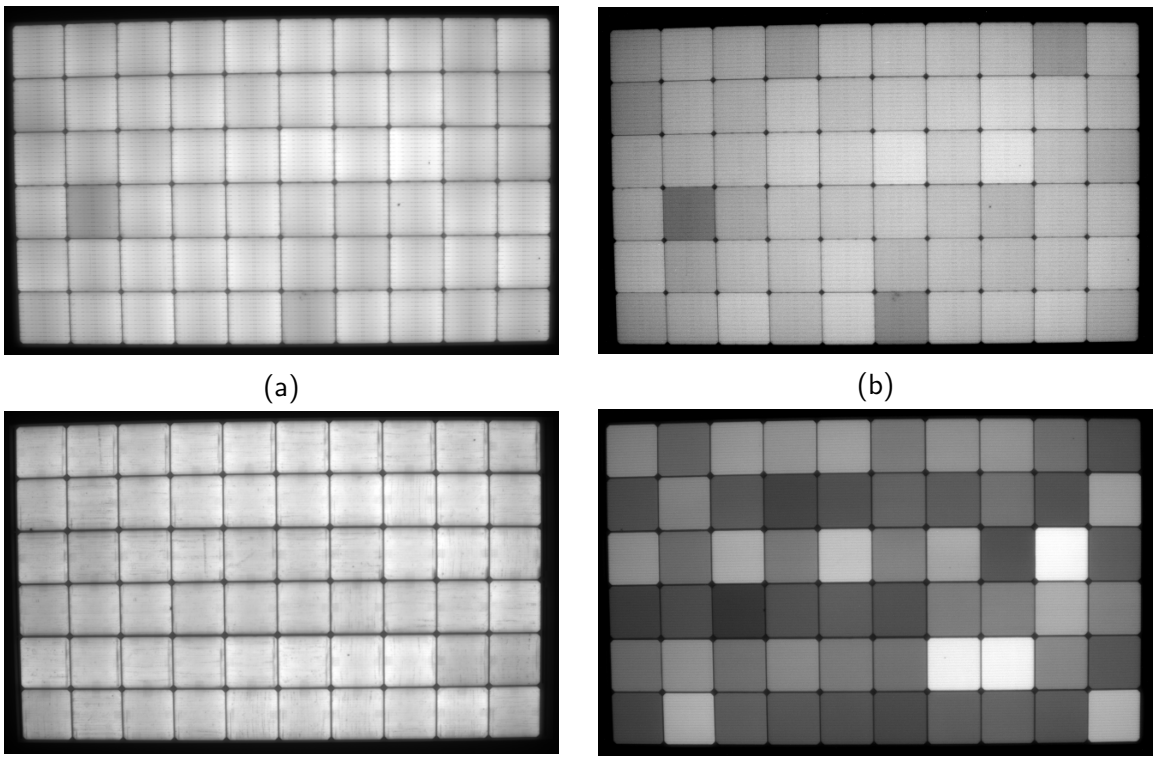

Figure 21: EL images taken at I_{sc} (left 21a and 21c) and 0,1 I_{sc} (right 21b and 21d) of each module after all LeTID rounds. a, b being EL images of Energetica module; c,d of Hevel module respectively. Pixel values are not changed, only the brightness and contrast are adjust for sharpening the images.

4.3 Alternative Stabilization Methods

In order to investigate the ordering behavior and stabilization further, thermal annealing and following light soaking were performed. The tables 7 and 8 represent electrical parameters of the modules after TA and LS respectively. STC measurements after TA and LS were followed by EL imaging shown in Figures 22 and 23 at forward currents of I_{sc} and 0,1 I_{sc}. No visible changes in EL images after both stabilization methods compared to previous procedures were obtained. Also the electric parameters listed in tables 7 and 8 showed no significant relative changes at power output: 0,1 % after TA and 0,1 % after LS in Hevel module, 0,5% after TA and 0,3% after LS in Energetica module.

Table 7: Electrical parameters at STC after TA for both modules. Multiflash measurements were done for Energetica module and DragonBack voltage profile was applied to the Hevel module for the measurement of the IV curve

Sample	V_{oc} [V]	I_{sc} [A]	P_{max} [W]	VatP_{max} [V]	IatP_{max} [A]	FF [%]
002005342000406E LeTID R3	40,82	9,74	312,1	33,6	9,29	78,51
190511129100003Q17el LeTID R3	43,73	9,16	309,3	36,22	8,54	77,22
002005342000406E	40,81	9,74	312,4	33,61	9,29	78,58
190511129100003Q17el	43,68	9,15	307,6	36,08	8,53	76,95

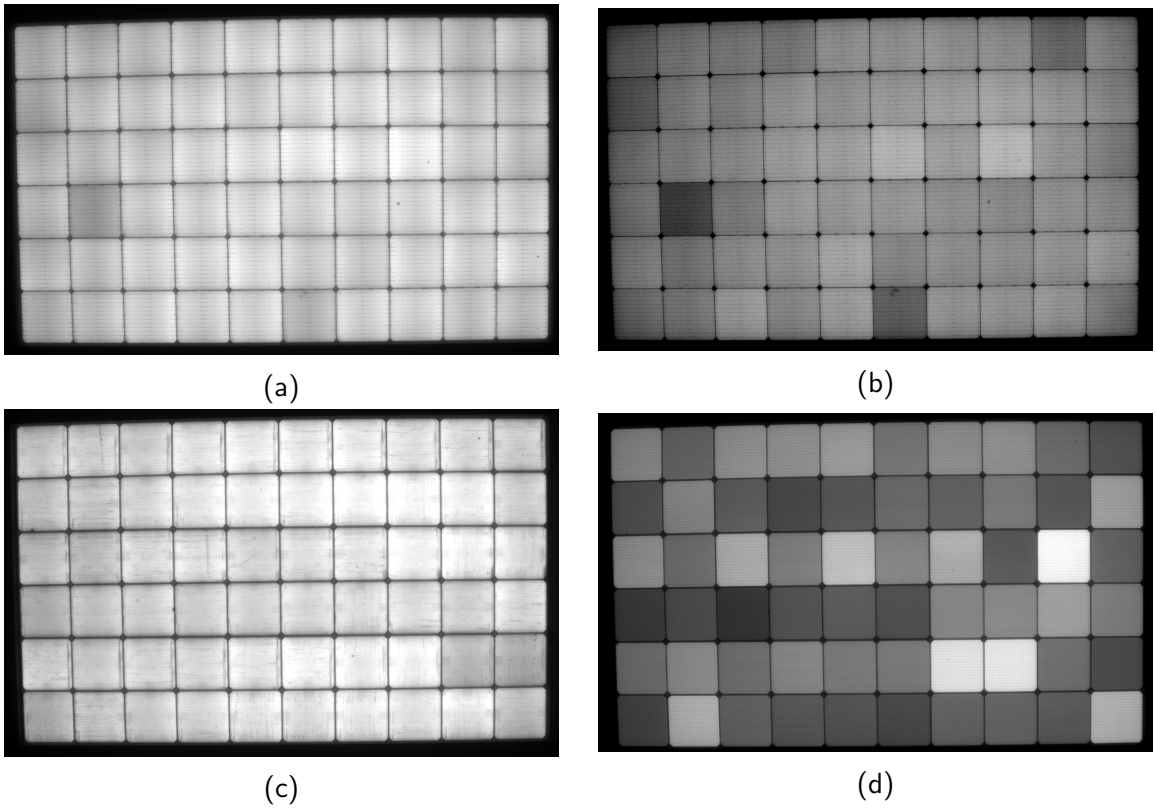

(a) (b) (c) (d)

Figure 22: EL images taken at I_{sc} (left 22a and 22c) and 0,1 I_{sc} (right 22b and 22d) of each module after TA. a, b being EL images of Energetica module; c,d of Hevel module respectively. Pixel values are not changed, only the brightness and contrast are adjust for sharpening the images.

Table 8: Electrical parameters at STC after LS for both modules. Multiflash measurements were done for Energetica module and DragonBack method was applied to Hevel module

Sample	V_{oc} [V]	I_{sc} [A]	P_{max} [W]	VatP_{max} [V]	IatP_{max} [A]	FF [%]
002005342000406E TA	40,81	9,74	312,4	33,61	9,29	78,58
190511129100003Q17el TA	43,68	9,15	307,6	36,08	8,53	76,95
002005342000406E	40,79	9,74	312,3	33,61	9,29	78,64
190511129100003Q17el	43,64	9,13	308,4	36,14	8,53	77,38

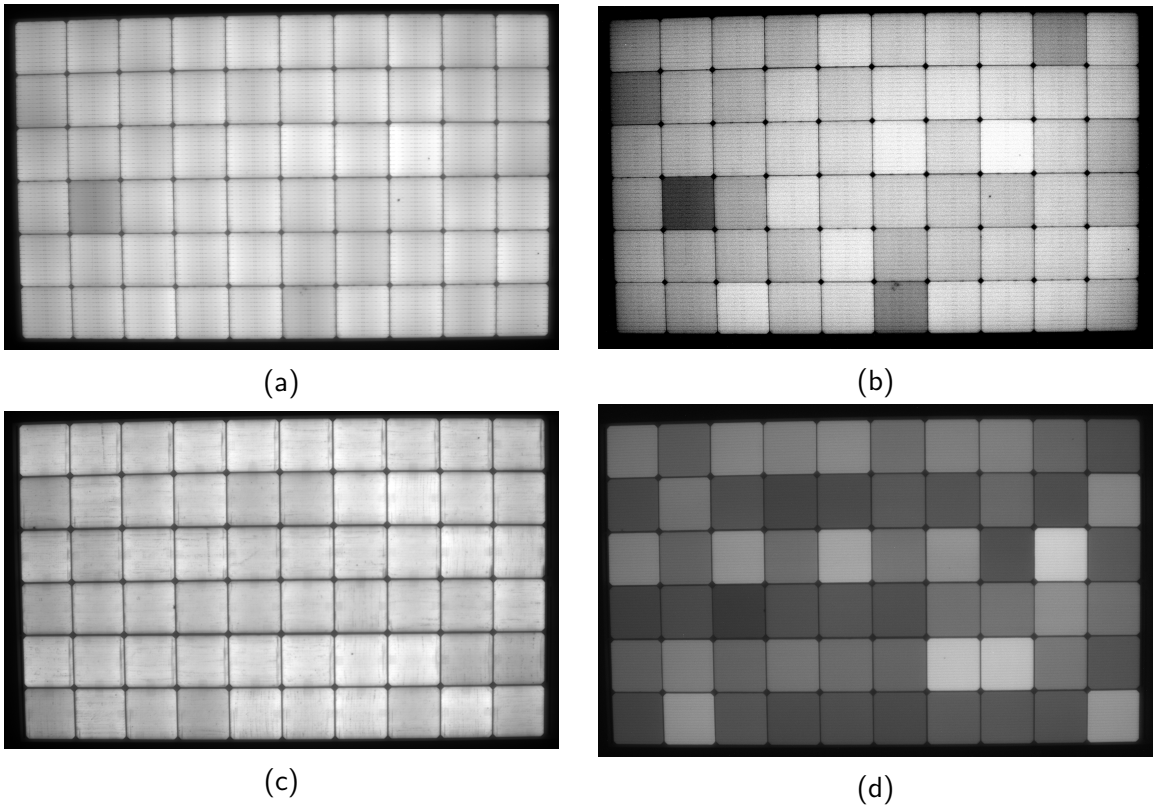

(a) (b) (c) (d)

Figure 23: EL images taken at I_{sc} (left 23a and 23c) and 0,1 I_{sc} (right 23b and 23d) of each module after LS. a, b being EL images of Energetica module; c,d of Hevel module respectively. Pixel values are not changed, only the brightness and contrast are adjust for sharpening the images.

4.4 Bias Stabilization

Series of forward bias rounds to see whether systematic increase in current injection affects response to this stabilization technique and aids to overall stabilization of modules were performed. Samples were to be stressed for three hours every round. Followed by STC IV curve measurements electrical pa-

rameters of 002005342000406E and 190511129100003Q17el are listed in the table 9 and 10 respectively.

Table 9: Electrical parameters at STC measured by multiflash measurements method after every round of forward bias of 002005342000406E

Bias [I_{sc}]	V_{oc} [V]	I_{sc} [A]	P_{max} [W]	V at P_{max} [V]	I at P_{max} [A]	FF [%]
LS	40,79	9,78	312,3	33,61	9,29	78,64
0,33	40,78	9,74	311,9	33,57	9,29	78,55
0,67	40,82	9,74	312,3	33,61	9,29	78,57
0,67	40,86	9,75	313,8	33,71	9,31	78,76
0,67	40,86	9,75	313,2	33,68	9,3	78,64
1	40,87	9,74	313,3	33,70	9,3	78,68
1	40,88	9,75	313,5	33,71	9,3	78,7
1	40,91	9,75	314	33,76	9,3	78,72
1	40,91	9,75	314,2	33,76	9,31	78,74
1	40,91	9,75	314,3	33,76	9,31	78,75
1	40,91	9,76	314,6	33,76	9,31	78,82
1	40,93	9,76	314,6	33,78	9,31	78,76
1	40,92	9,76	314,5	33,77	9,31	78,78
1,33	40,93	9,76	314,5	33,78	9,31	78,77
1,33	40,94	9,76	314,7	33,8	9,31	78,79
1,33	40,93	9,76	314,8	33,8	9,31	78,81
1,33	40,94	9,76	314,8	33,8	9,31	78,78
1,33	40,94	9,76	315,1	33,82	9,32	78,85
1,33	40,95	9,76	315,1	33,82	9,32	78,82
1,33	40,96	9,76	315,1	33,83	9,32	78,81
1,67	40,94	9,76	314,8	33,78	9,32	78,76
1,67	40,94	9,76	314,4	33,76	9,31	78,71
1,67	40,94	9,76	314,3	33,76	9,31	78,66

Table 10: Electrical parameters at STC measured by DragonBack method after every round of forward bias of 190511129100003Q17el

Bias [I_{sc}]	V_{oc} [V]	I_{sc} [A]	P_{max} [W]	VatP_{max} [V]	IatP_{max} [A]	FF [%]
LS	43,64	9,13	308,4	36,14	8,53	77,38
0,33	43,69	9,15	308,9	36,2	8,53	77,29
0,67	43,74	9,15	309,5	36,29	8,53	77,37
0,67	43,74	9,15	309,7	36,27	8,54	77,36
0,67	43,77	9,16	309,8	36,3	8,53	77,3
1	43,78	9,15	310	36,31	8,54	77,36
1	43,73	9,15	309,6	36,27	8,54	77,33
1	43,78	9,16	310	36,32	8,54	77,33
1	43,82	9,15	310,1	36,33	8,54	77,38
1	43,78	9,15	309,8	36,3	8,54	77,37
1,33	43,8	9,16	310	36,3	8,54	77,28
1,33	43,81	9,16	310	36,31	8,54	77,27
thermal stress						
1,33	43,81	9,16	309,6	36,26	8,54	77,18
1,33	43,84	9,15	309,4	36,28	8,53	77,13
1,33	43,84	9,16	309,8	36,28	8,54	77,17
1,33	43,84	9,16	309,7	36,27	8,54	77,15
1,67	43,9	9,16	310,2	36,33	8,54	77,19
1,67	43,84	9,16	310	36,3	8,54	77,17

Graphical representations of absolute P_{max} of both samples over exposure time during bias routes are shown in Figure 24. During the first set (i.e. consecutive application of biasing followed by STC measurement or the electric parameters) of biasing intervals at a given current of 0,67 I_{sc} the system started to show ordering dynamics. As soon as the main ordering parameter, current, was increased, the system was again starting to order towards the new thermodynamic equilibrium for the new ordering parameters, as given with the current values for biasing in tables 9 and 10.

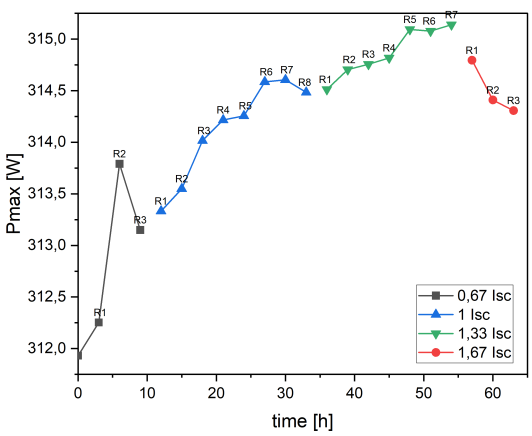

(a) 002005342000406E

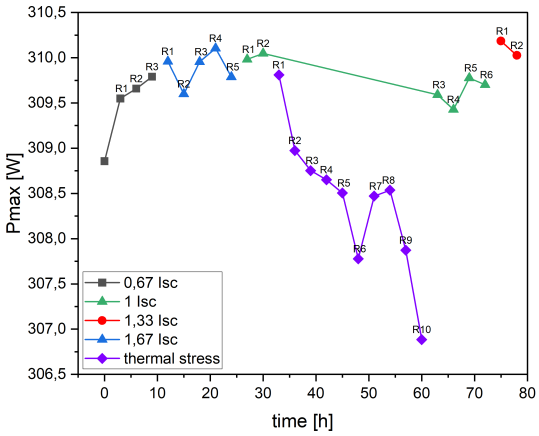

(b) 190511129100003Q17el

Figure 24: Systematic changes of absolute power over exposure time during first three rounds of Energetica module are illustrated in caption 24a. Systematic changes of absolute power over exposure time during first three rounds with pause of approximately two months for thermal stress between R2 (green ▲) and R3 (green ▲) of Hevel module are illustrated in caption 24b. Starting from the last bias cycle of 1,67 I_{sc} (red •) in both captions, the mechanism was switched and no systematic changes were obtained. The lines are for guidance of the eyes.

The Figure 25 shows relative changes in electrical parameters of both modules after every bias round and thermal stress. Main changes of both samples are to be seen in P_{max} performance. After the modules were operated at 1,67 I_{sc}, the system was put in disordered state and no systematic changes were observed. P_{max} values are negative and the samples show degrading effects.

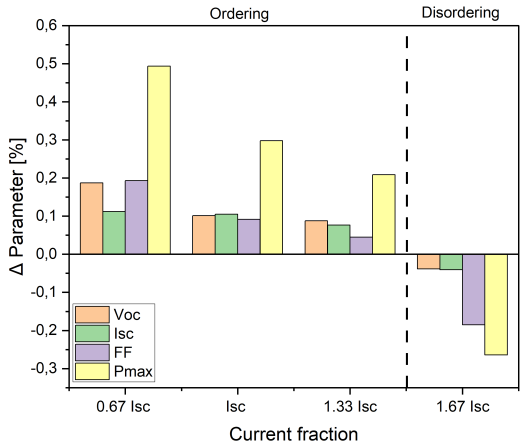

(a) 002005342000406E

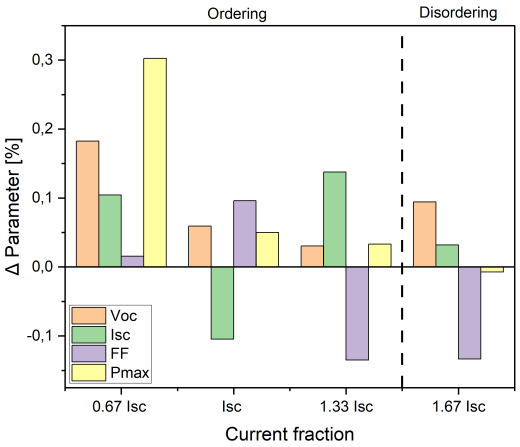

(b) 190511129100003Q17el

Figure 25: Relative changes of electrical parameters of the samples. Both caption 25a and caption 25b illustrate decreasing behaviour of P_{max}. Systematic changes occur for current values from 0,67 Isc to 1,33 Isc, after that the mechanism of the system may have changed and a disordered state with negative P_{max} values is obtained. The dashed lines are for visual separation of two states.

STC measurements after all bias rounds were followed by EL imaging. Pictures shown in Figure 26 at forward currents of I_{sc} and 0,1 I_{sc} are from last bias round of each module. No visible changes in EL images after forward bias stabilization method compared to previous procedures were obtained.

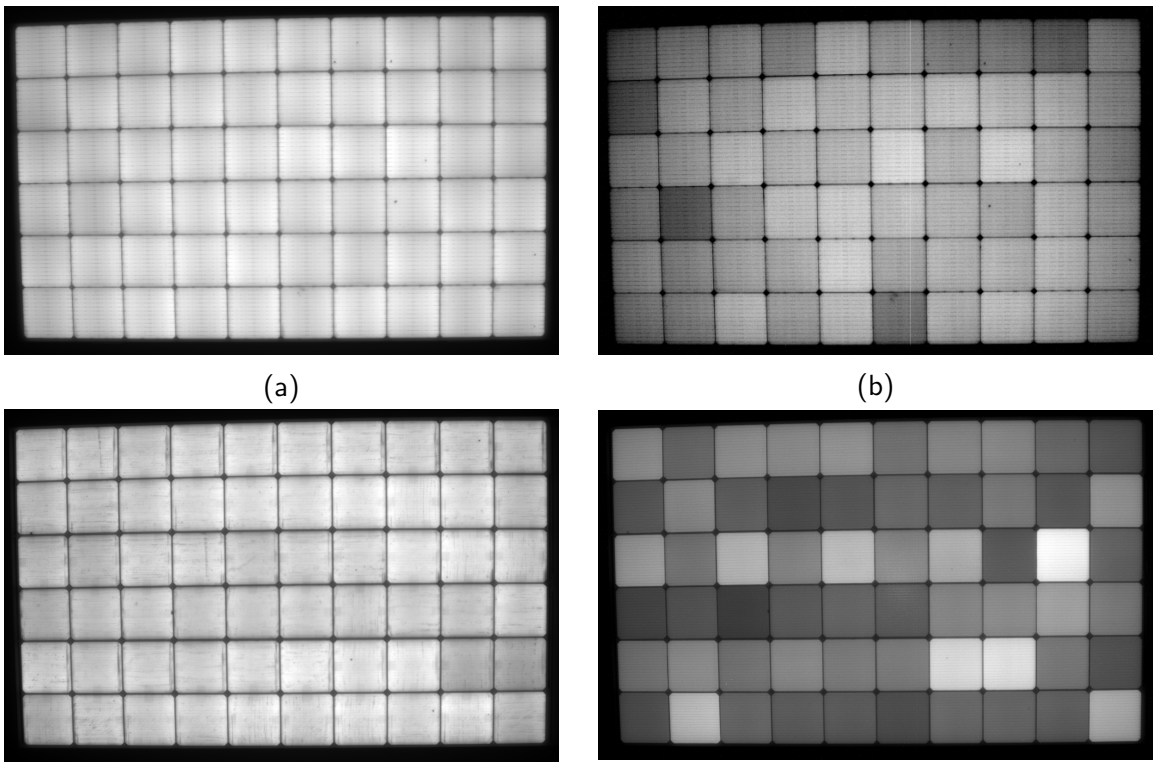

(a) (b)

(c) (d)

Figure 26: EL images taken at I_{sc} (left 26a and 26c) and 0,1 I_{sc} (right 26b and 26d) of each module after last round of current injection. a, b being EL images of Energetica module; c,d of Hevel module respectively. Pixel values are not changed, only the brightness and contrast are adjusted for sharpening the images.

4.5 Arrhenius Behaviour

Figure 24 shows the systematic changes of absolute power over exposure time during first three bias rounds. In order to identify the correct values for the Arrhenius plot, saturation points needed to be chosen correctly. This was even harder considering that the relative changes for the power output are below 0,5 % (see Figure 25). For the given data it was seen critical to just analyse the raw data as this was strongly noisy. Also, there was not enough data to do an appropriate saturation fit. Therefore, conservative values, which might support a smooth saturating behavior at each fixed current value were chosen. This was done as follows: the saturation point for the first bias round at 0,67 I_{sc} of Energetica module in Figure 24a is neither R2 (black curve) nor R3 (black curve), but the average of both. Similar behaviour with sharp peaks can also be obtained in the behaviour of Hevel module shown in Figure 24b at 1 I_{sc}.

Similarly, the final saturation point at 1 I_{sc} was chosen as the average value of R4 (blue curve) and R5 (blue curve). For the reason that the relative changes are small, one could interpret such peaks (R1-R5 of Hevel module, blue curve) as fluctuations. For the saturation value at 1,33 I_{sc} of the green curve of Hevel module R2 was chosen. In spite of the fact that after thermal stress the sample was further operated at 1,33 I_{sc}, points from R3 to R6 are not taken into account. The reason is, that during thermal stabilization the module underwent different mechanism and the system was in a different degree of order.

Values for 1,67 I_{sc} were not taken into account for Arrhenius plot of both samples. The cause is that the system goes into a disordered state and no systematic changes were obtained. High current injection may cause change of the mechanism, which shows a degrading effect. Arrhenius plots of the logarithmic averaged variable (P) on the y-axis and inverse short circuit current (1000/I_{sc}) on the x-axis are represented in Figure 27a of Energetica module and in Figure 27b of Hevel module. The values used to plot the curves are listed in table 11. As mentioned above for some bias rounds initial and final points had to be adjusted to allow a meaningful fit.

Table 11: contains the averaged variable (P_{max}), its logarithm and bias values as short circuit current fractions of Energetica (left side) and Hevel (right side) modules

Bias [I_{sc}]	ΔP_{max} [W]	lnΔP
0,67	1,54	0,43
1	0,94	-0,06
1,33	0,66	-0,42

Bias [I_{sc}]	ΔP_{max} [W]	lnΔP
0,67	0,93	-0,07
1	0,16	-1,86
1,33	0,07	-2,71

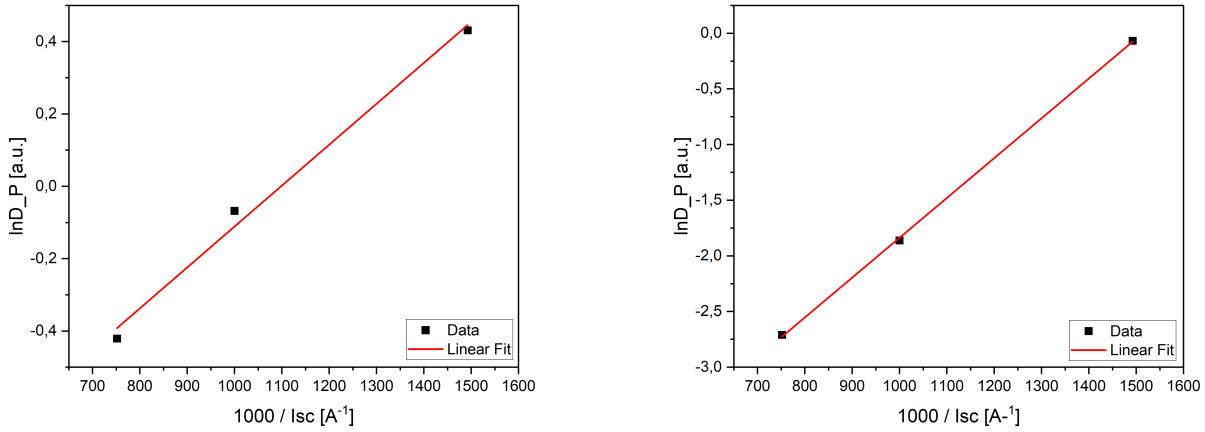

(a) 002005342000406E (b) 190511129100003Q17el

Figure 27: Arrhenius behaviour of averaged power (■) over time during biasing as a function of inverse current. Caption 27a shows Arrhenius behaviour of Energetica module and caption 27b of Hevel module, respectively. The red solid lines represent the linear fit.

5 Discussion and Outlook

In this work, we investigated the behaviour of two PV modules with different c-Si cell technologies (PERC and HJT) under indoor experiments. When interpreting the results, it should be kept in mind, that the range of stabilization procedures can differ depending on the module history, stabilization time and measurement technique. According to the international inter-laboratory study on LeTID [34] after four weeks of carrier injection (I_{sc} – I_{mp}) at 75°C LeTID could be detected. On the other hand, the IEC TS 63342 protocol, in order to double the initial degradation rate, reduces the test procedure used by [34] to two weeks, and accelerates the initial phase of LeTID by doubling the dark current injection to $2(I_{sc} - I_{mp})$. We followed the TS protocol and applied doubled injection current.

As mentioned in a previous section dark IV in-situ measurements during an ongoing LeTID test together with interim IV measurements at STC were done. Without these measurements it may have happen that the degradation followed by recovery might have shown after several weeks almost the initial power out-

put, but missing the previous degradation. With the setup chosen, the interim measurements would detect such degradation. However, after a sufficiently long period of time (approximately three weeks), which should allow a complete LeTID degradation phase, no significant power change ($\Delta P_{Energetica} = 0,67\%$ and $\Delta P_{Hevel} = 1,75\%$) was seen. Therefore, the system was examined in terms of its stability to order parameters and transition mechanisms. As explained in section 3.4.1 for LeTID we used both current injection and temperature stabilization. Being two different energy sources they activate different mechanisms. Temperature may affect an order state in different ways allowing disorder-order or order-disorder transitions. The current injection, on the contrary, when being in a highly ordered state allow order-disorder, leading to degradation. On the other hand, if the system was in a disordered state, like some thin-film modules, then the current injection leads to ordering. It is important to mention, that samples may also be too well ordered for a given temperature and the temperature itself does not have enough activation energy to order the system. The two parametes combined, obviously, show some changes, but they are too long-range and have such a small amplitude that we cannot observe them, furthermore we do not know which of the mechanisms is suppressed in LeTID. Since that, we decided to isolate one parameter and see if the system responds to that parameter.

Firstly, TA was performed without current injection or illumination. Then, for LS, instead, illumination was applied, but the temperature was reduced and there was no current injection. Finally, for the bias stabilization method the temperature value was put to 75°C, the same as for LeTID and the current injection value was systematically increased in 1/3 I_{sc} fractions. For this two commercial modules details of cell architecture and doping processes are not disclosed. Both samples did not show LeTID effect, yet they systematically responded to changes in order parameter with both order and disorder. This can be obtained by applying Arrhenius characteristic curves, shown in Figure 27. By changing a mechanism we could see whether the system reacts to changes in order or disorder parameters. These changes can be explained by an increasing number of point defects like vacancies and self-interstitials. As soon as most defects are healed (in our case by current injection) and the

system receives more energy (in our case thermal), new defects arrange again, resulting in reduction of modules' performance.

The interval of power changes until stabilization decrease while the current values for biasing increase. The reason is that the system already shifted in its order dynamics to the disordering regime for current values above 1,33 I_{sc}. The mechanisms follow Boltzmann statistics which was proven by the Arrhenius like behaviour in the previous section, i.e. to achieve similar changes in the ordering mechanism the higher current injection value is needed. The interpretation can be made that most probably the origin of this Arrhenius-like behaviour is changed in the point defect structure and therefore interaction with the intrinsic parameters of the solar cell. The mechanism is an "order-order" relaxation driven by the increasing current and/or activation of point defects. We conclude that the regime for the first three rounds of bias was not switched, because decrease in the power output during thermal stress amid bias stabilization procedure demonstrates that systematic current injections led to ordering. One can easily see that the system follows Arrhenius behaviour and order-order transition happens due to dark bias as shown in Figure 27 and described in section 4.5. Nevertheless above a certain current value the mechanism is changed and the system switches to a disordered state as depicted in Figure 25. From the course of red points in both Figure 24a and Figure 24b one can see that limits of the system are achieved and from this point on the mechanism is switched and system is going to order-disorder state. This means that at a certain point of increasing the current, the underlying mechanism brakes down or another mechanism is energetically favorable leading to an order-disorder dynamics. This is clearly seen in the deviation of the power-change from Arrhenius behavior as well as continuous degradation of the modules power. Note, that except of a further increase of current, all other parameters for the experiment were stable.

For the reason that our samples were not treated on the microscopic scale and only macroscopic indicators were studied, the interpretation of results is obtained from observed electrical parameters. It could be relevant to investigate samples on the microscopic scale to be able to determine whether mech-

anisms activated by current injection, temperature or both combined are ordering or disordering mechanisms. Since dark bias stabilization is cost effective and time consuming, because more modules can be kept in the same climatic chamber at dark bias, when compared to light driven testing where the area of the stationary sun simulator limits the number of simultaneous treated modules. Therefore it is a good alternative for both manufacturers and research. LeTID has only been observed relatively recently [24] and still not well understood. IEC Technical Specification protocol differs from the procedure used in the inter-laboratory test, primarily in the current injection value. Certainly finely tuned accelerating testings and more research work is needed in pursuance of better understanding of underlying processes.

List of Abbreviations

AIT austrian institute of technology.

Al-BSF aluminum back surface field.

AM air mass.

ARC anti reflective coating.

c-Si crystalline silicon.

CCD charge coupled device.

EL electroluminescence.

Ge germanium.

HDI human developing index.

HJT heterojunction.

IEC international electrotechnical commission.

LeTID light- and elevated temperature-induced degradation.

LID light induced degradation.

LS light soaking.

MQT module quality tests.

NIR near-infrared.

PERC passivated emitter and rear contact.

PV photovoltaic.

Si silicon.

STC standard test condition.

TA thermal annealing.

TS technical specification.

TÜV technischer überwachungs-Verein.

References

[1] P. Würfel. *Physics of Solar Cells: From Basic Principles to Advanced Concepts*. Physics textbook. Wiley, 2009. ISBN: 9783527408573. URL: https://books.google.at/books?id=w6Ii4r7FuskC.

[2] D. Neamen. *Semiconductor Physics And Devices*. McGraw-Hill Series in Electrical and Computer Engineering. McGraw-Hill Education, 2003. ISBN: 9780072321074. URL: https://books.google.at/books?id=TPE9AQAAIAAJ.

[3] Stephen G. Benka. "The Energy Challenge". In: *Physics Today* 55.4 (2002), pp. 38–39. DOI: https://doi.org/10.1063/1.1480780.

[4] Alan D Pasternak. "Global energy futures and human development: a framework for analysis". In: (2001).

[5] A. E. Becquerel. "Memoire sur les Effects d'Electriques Produits Sous l'Influence des Rayons Solaires". In: *Comptes Rendus* 9 (1839), pp. 561–567.

[6] W.G. Adams and R.E. Day. "The Action of Light on Selenium". In: *Proceedings of the Royal Society, London* A25 (1877). ¡br /¿, p. 113.

[7] Albert Einstein. "Zur Quantentheorie der Strahlung. (German) [On the Quantum Theory of Radiation]". In: 18 (1917), pp. 121–128.

[8] D. M. Chapin, C. S. Fuller, and G. L. Pearson. "A New Silicon p-n Junction Photocell for Converting Solar Radiation into Electrical Power". In: *Journal of Applied Physics* 25.5 (1954), pp. 676–677. DOI: 10.1063/1.1721711. eprint: https://doi.org/10.1063/1.1721711. URL: https://doi.org/10.1063/1.1721711.

[9] Daryl M. Chapin Gerald L. Pearson and Calvin S. Fuller(AT&T). "SSolar Energy Converting Apparatus"". U.S. pat. 2780765. 1957.

[10] J. L. Nayler. "Vanguard. A History. Constance M. Green and Milton Lomask. NASA Historical Series (SP 4202). Paperback. Illustrated. 308 pp." In: *The Aeronautical Journal (1968)* 75.730 (1971), pp. 742–742. DOI: 10.1017/S0001924000046601.

[11] Simon Min Sze. *Semiconductor devices: physics and technology*. John wiley & sons, 2008.

[12] M.A. Green. *Solar Cells: Operating Principles, Technology, and System Applications*. Prentice-Hall Contemporary Comparative Politics Series. Prentice-Hall, 1982. ISBN: 9780138222703. URL: https://books.google.at/books?id=ODAEAQAAIAAJ.

[13] P.D. Davis, G.D. Parbrook, and G.N.C. Kenny. "CHAPTER 7 - Diffusion and Osmosis". In: *Basic Physics and Measurement in Anaesthesia (Fourth Edition)*. Ed. by P.D. Davis, G.D. Parbrook, and G.N.C. Kenny. Fourth Edition. Butterworth-Heinemann, 1995, pp. 89–102. ISBN: 978-0-7506-1713-0. DOI: https://doi.org/10.1016/B978-0-7506-1713-0.50012-3. URL: https://www.sciencedirect.com/science/article/pii/B9780750617130500123.

[14] Arvind Shah. *Solar Cells and Modules*. Jan. 2020. ISBN: 978-3-030-46485-1. DOI: 10.1007/978-3-030-46487-5.

[15] Martin A Green and Mark J. Keevers. "Optical properties of intrinsic silicon at 300 K". In: *Progress in Photovoltaics: Research and Applications* 3 (1995 1995). ¡br /¿, pp. 189–192. ISSN: 1099159X. DOI: 10.1002/pip.4670030303.

[16] Hala J. El-Khozondar et al. "Modified solar cells with antireflection coatings". In: *International Journal of Thermofluids* 11 (2021), p. 100103. ISSN: 2666-2027. DOI: https://doi.org/10.1016/j.ijft.2021.100103. URL: https://www.sciencedirect.com/science/article/pii/S2666202721000410.

[17] Mu Xiao et al. "Recent advances of metal-oxide photoanodes: engineering of charge separation and transportation toward efficient solar water splitting". In: *Solar RRL* 4.8 (2020), p. 1900509.

[18] Jingxiang Low et al. "Heterojunction photocatalysts". In: *Advanced materials* 29.20 (2017), p. 1601694.

[19] Shengnan Li et al. "Recent Progress on Semiconductor Heterojunction-Based Photoanodes for Photoelectrochemical Water Splitting". In: *Small Science* 2.5 (), p. 2100112.

[20] D. Dirnberger. "2 - Photovoltaic module measurement and characterization in the laboratory". In: *The Performance of Photovoltaic (PV) Systems*. Ed. by Nicola Pearsall. Woodhead Publishing, 2017, pp. 23–70. ISBN: 978-1-78242-336-2. DOI: https://doi.org/10.1016/B978-1-78242-336-2.00002-1. URL: https://www.sciencedirect.com/science/article/pii/B9781782423362000021.

[21] N. Ferretti et al. "Performance Testing of High-Efficient PV Modules Using Single 10 ms Flash Pulses". In: 2013, pp. 3184–3187. ISBN: 3-936338-33-7. DOI: 10.4229/28thEUPVSEC2013-4AV.5.4. URL: https://www.eupvsec-proceedings.com/proceedings?paper=23010.

[22] Iea Pvps et al. "Review on Infrared and Electroluminescence Imaging for PV Field Applications". In: 2018. ISBN: 3-936338-50-7. DOI: 10.4229/35thEUPVSEC20182018-6DP.2.4.

[23] International Electrotechnical Commission. *Photovoltaic devices - Part 13: Electroluminescence of photovoltaic modules*. en. Standard. Geneva, CH: International Electrotechnical Commission, 2018-08-29. URL: https://webstore.iec.ch/publication/26703&preview.

[24] Klaus Ramspeck et al. "Light induced degradation of rear passivated mc-Si solar cells". In: *Proceedings of the 27th European Photovoltaic Solar Energy Conference and Exhibition*. 2012.

[25] Fabian Fertig, Karin Krauß, and Stefan Rein. "Light-induced degradation of PECVD aluminium oxide passivated silicon solar cells". In: *physica status solidi (RRL)–Rapid Research Letters* 9.1 (2015), pp. 41–46.

[26] Tabea Luka, Marko Turek, and Christian Hagendorf. "Defect formation under high temperature dark-annealing compared to elevated temperature light soaking". In: *Solar Energy Materials and Solar Cells* 187 (2018), pp. 194–198. ISSN: 0927-0248. DOI: https://doi.org/10.1016/j.solmat.2018.06.043. URL: https://www.sciencedirect.com/science/article/pii/S0927024818303544.

[27] Wolfram Kwapil et al. "Temporary Recovery of the Defect Responsible for Light- and Elevated Temperature-Induced Degradation: Insights Into the Physical Mechanisms Behind LeTID". In: *IEEE Journal of Photovoltaics* 10.6 (2020), pp. 1591–1603. DOI: 10.1109/JPHOTOV.2020.3025240.

[28] Hang Cheong Sio et al. "The Role of Dark Annealing in Light and Elevated Temperature Induced Degradation in p-Type Mono-Like Silicon". In: *IEEE Journal of Photovoltaics* 10.4 (2020), pp. 992–1000. DOI: 10.1109/JPHOTOV.2020.2993653.

[29] Fokuhl, Esther et al. "LID and LETID evolution of PV modules during outdoor operation and indoor tests". In: *EPJ Photovolt.* 12 (2021), p. 9. DOI: 10.1051/epjpv/2021009. URL: https://doi.org/10.1051/epjpv/2021009.

[30] Svenja Wilking et al. "From simulation to experiment: Understanding BO-regeneration kinetics". In: *Solar Energy Materials and Solar Cells* 142 (2015), pp. 87–91.

[31] Wolfram Kwapil, Tim Niewelt, and Martin C. Schubert. "Kinetics of carrier-induced degradation at elevated temperature in multicrystalline silicon solar cells". In: *Solar Energy Materials and Solar Cells* 173 (2017). Proceedings of the 7th international conference on Crystalline Silicon Photovoltaics, pp. 80–84. ISSN: 0927-0248. DOI: https://doi.org/10.1016/j.solmat.2017.05.066. URL: https://www.sciencedirect.com/science/article/pii/S092702481730301X.

[32] Dennis Bredemeier, Dominic Walter, and Jan Schmidt. "Light-induced lifetime degradation in high-performance multicrystalline silicon: Detailed kinetics of the defect activation". In: *Solar Energy Materials and Solar Cells* 173 (2017). Proceedings of the 7th international conference on Crystalline Silicon Photovoltaics, pp. 2–5. ISSN: 0927-0248. DOI: https://doi.org/10.1016/j.solmat.2017.08.007. URL: https://www.sciencedirect.com/science/article/pii/S0927024817304452.

[33] E. Fokuhl et al. "LeTID - A Comparison of Test Methods on Module Level". In: 2019, pp. 816–821. ISBN: 3-936338-60-4. DOI: 10.4229/EUPVSEC20192019-4BO.12.2. URL: https://www.eupvsec-proceedings.com/proceedings?paper=48290.

[34] Joseph Karas et al. "Results from an international interlaboratory study on light- and elevated temperature-induced degradation in solar modules". In: *Progress in Photovoltaics: Research and Applications* 30.11 (2022), pp. 1255–1269. DOI: https://doi.org/10.1002/pip.3573. eprint: https://onlinelibrary.wiley.com/doi/pdf/10.1002/pip.3573. URL: https://onlinelibrary.wiley.com/doi/abs/10.1002/pip.3573.

[35] International Electrotechnical Commission. *C-Si photovoltaic (PV) modules – Light and elevated temperature induced degradation (LETID) test – Detection*. en. Standard. Geneva, CH: International Electrotechnical Commission, 2022-07-20.

[36] W. Ananda et al. "Alternate stabilization methods for CZTSSe photovoltaic devices by thermal treatment, dark electric bias and illumination". In: *Solar Energy* 245 (2022), pp. 299–307. ISSN: 0038-092X. DOI: https://doi.org/10.1016/j.solener.2022.08.056. URL: https://www.sciencedirect.com/science/article/pii/S0038092X22006077.

[37] Michael Gostein and Larry Dunn. "Light soaking effects on photovoltaic modules: Overview and literature review". In: *Conference Record of the IEEE Photovoltaic Specialists Conference* (June 2011), pp. 003126–003131. DOI: 10.1109/PVSC.2011.6186605.

[38] C Deline et al. "Electrical Bias as an Alternate Method for Reproducible Measurement of Copper Indium Gallium Diselenide (CIGS) Photovoltaic Modules: Preprint". In: 8472 (Aug. 2012). ISSN: 0277-786X. DOI: 10.1117/12.929899. URL: https://www.osti.gov/biblio/1050147.

[39] Mittal, Ankit et al. "Power change in amorphous silicon technology by low temperature annealing". In: *EPJ Photovolt.* 6 (2015), p. 65304. DOI: 10.1051/epjpv/2015007. URL: https://doi.org/10.1051/epjpv/2015007.